materials

MDPI

Review

Recent Advances in Photo-Responsive Microencapsulated Phase-Change Materials

Chaofeng Yang and Binyang Du *

State Key Laboratory (SKL) of Biobased Transportation Fuel Technology, Department of Polymer Science & Engineering, Zhejiang University, Hangzhou 310058, China; 22329009@zju.edu.cn
* Correspondence: duby@zju.edu.cn

Abstract

Photo-responsive microencapsulated phase-change materials (MEPCMs) are attracting growing interest for their significant potential in solar energy applications and advanced intelligent thermal management systems, owing to their exceptional capacity for thermal energy storage, efficiency for photothermal conversion, and capability for multifunctional integration. This review provides a systematic summary of the advancements in photo-responsive MEPCMs containing photothermal, photocatalytic, and luminescent materials in the past five years, highlighting their potential in energy conversion, pollutant degradation, and intelligent sensing applications. Moreover, perspectives for future research are provided to enhance the practical application of photo-responsive MEPCMs.

Keywords: phase-change materials; microcapsule; photo-responsiveness; multifunctionality

check for updates

Academic Editor: Antonio Caggiano

Received: 25 September 2025
Revised: 30 October 2025
Accepted: 31 October 2025
Published: 3 November 2025

Citation: Yang, C.; Du, B. Recent Advances in Photo-Responsive Microencapsulated Phase-Change Materials. *Materials* **2025**, *18*, 5014. https://doi.org/10.3390/ma18215014

Copyright: © 2025 by the authors. Licensee MDPI, Basel, Switzerland. This article is an open access article distributed under the terms and conditions of the Creative Commons Attribution (CC BY) license (https://creativecommons.org/licenses/by/4.0/).

1. Introduction

With the continuous growth of global consumption, environmental pollution and energy shortages are becoming increasingly severe, posing higher requirements for energy efficiency [1,2]. Therefore, thermal energy storage (TES) technologies have received widespread attention and emerged as a significant research area [3,4]. Traditional TES technologies are mainly categorized into latent heat storage (LHS) [5–9], thermal chemical heat storage (TCHS) [10–12], and sensible heat storage (SHS) [13–15]. Compared with SHS (which typically has lower energy density) and TCHS (which depends on chemical reactions), LHS has attracted considerable research attention owing to its favorable safety profile and high energy storage density. Phase-change materials (PCMs) [16–19], often referred to as LHS materials, exhibit high phase-change enthalpies, enabling them to release and absorb substantial thermal energy with minimal temperature variation during phase transitions.

However, the considerable volumetric variation and leakage tendencies during the phase transition process notably hinder the practical deployment of PCMs, especially the most widely used solid-to-liquid PCMs [20,21]. To solve these challenges, the microencapsulation technique has been widely adopted as an effective approach to stabilize PCMs [22]. This technique not only effectively mitigates the risk of leakage during thermal cycling but also enhances the specific surface area of PCMs, thereby markedly improving their thermal response rate and transfer performance [23]. With the continuous advancements of microencapsulation technologies, increasing efforts have been devoted to incorporating various functional materials into the shell of microencapsulated phase-change materials

(MEPCMs), as well as embedding specific nanoparticles in both shell and core regions, aiming to endow MEPCMs with diversified functionalities [24–27].

In the past few years, the emergence of photo-responsive materials has introduced new opportunities for the advancement of MEPCMs [28]. These materials enhance the utilization efficiency of solar energy and impart additional functional attributes, thereby accelerating the development of MEPCMs toward multifunctionality. This review provides a systematic compilation of the latest research and application status of photo-responsive MEPCMs containing photothermal, photocatalytic, or luminescent materials, with a specific emphasis on their manufacturing techniques, functional mechanisms, recent breakthroughs, and future development directions.

2. Microencapsulated Phase-Change Materials (MEPCMs)

MEPCMs feature a core–shell architecture, in which PCMs serve as the encapsulated core, while the protective shell is constructed from inorganic compounds [29,30], polymeric materials [31,32], or metals and their alloys [33]. The microcapsules are prepared via a core–shell strategy. The core, such as paraffin wax, is dispersed in water to form droplets, and a shell—either inorganic (e.g., $CaCO_3$), organic (e.g., polymer), or hybrid—is formed around the droplets via in situ polymerization, interfacial polymerization, or sol–gel methods. Functional nanoparticles such as TiO_2 can be incorporated into the shell to provide additional properties, such as photocatalytic activity. This particulate architecture enables stable and efficient TES. The PCM cores absorb or release substantial thermal energy, thereby facilitating effective energy storage and utilization. PCMs can be divided into two primary categories: organic materials and inorganic materials, depending on their chemical compositions. Organic PCMs primarily include paraffins (saturated hydrocarbons) [34,35], fatty acids [36,37], and their eutectic mixtures [38], as well as polyols. These materials are characterized by chemical inertness, non-toxicity, non-corrosiveness, and a diverse spectrum of phase-transition temperatures, which render them highly appropriate for TES in low- to medium-temperature applications. For instance, *n*-alkanes derived from paraffin waxes exhibit remarkable latent heat capacity, cost-effectiveness, and reliable thermal stability, and they are therefore frequently employed as organic candidates [39]. Apart from paraffin-based materials, non-paraffinic ones such as fatty acids also demonstrate high latent heat, excellent chemical stability, minimal volume variation during phase transitions, and low susceptibility to supercooling. In addition, by blending different types of organic PCMs in specific ratios to form eutectic mixtures, the phase-transition temperature is capable of being flexibly adjusted to meet the demands of specific target applications. However, organic PCMs suffer from inherent drawbacks, including low thermal conductivity, high flammability, and relatively low material density. A lower material density means that less PCM mass is contained within a given volume, resulting in a lower volumetric energy storage capacity. These shortcomings collectively limit their suitability for high-efficiency thermal storage systems. Inorganic PCMs mainly consist of salt hydrates [40] and metals and their alloys [41–44]. Salt hydrates, composed of water and inorganic salts of crystallization, typically offer remarkable latent heat, moderate thermal conductivity, and low cost, making them one of the most widely utilized categories of inorganic PCMs. Moreover, the relatively remarkable thermal storage density of salt hydrates renders them appropriate for TES applications in the low-to-medium temperature range. However, these materials also exhibit notable drawbacks, including corrosiveness toward metallic components, as well as a tendency to undergo supercooling and phase separation during phase transitions—factors that adversely affect their thermal storage performance and cycling stability [45]. Another class of inorganic PCMs includes metals and their alloys, such as gallium (Ga) and its alloys [46,47] for low-temperature applications, as well as tin

(Sn) [48,49], bismuth (Bi) [50], copper (Cu) [51], aluminum (Al) [52,53], etc., for medium- to high-temperature TES. These materials provide excellent thermal conductivity, good reversibility, and high thermal stability during melting and solidification. Therefore, they are regarded as ideal candidates for high energy density and efficient thermal storage. Despite their superior heat transfer performance, metal-based PCMs generally possess lower latent heat per unit mass and involve higher material costs, which limit their feasibility for large-scale TES systems. In general, organic PCMs are more suitable for low-temperature applications where chemical stability, low cost, and non-corrosiveness are required. Inorganic PCMs—particularly salt hydrates and metals and their alloys—are preferred in systems demanding higher thermal conductivity and volumetric energy density. The major differences between organic and inorganic PCMs in terms of their thermophysical properties, advantages, and typical application domains are summarized in Table 1.

Table 1. Comparison between organic and inorganic PCMs under different operating conditions.

Category	Typical Materials	Melting Range	Advantages	Limitations	Representative Applications
Organic PCMs	Paraffins [34,35], polyols, fatty acids [36,37]	Low- to medium-temperature (typically <200 °C)	Chemically stable, non-corrosive, low cost, adjustable melting point	Low thermal conductivity, flammable, low density	Building thermal regulation, textiles, packaging
Inorganic PCMs	Salt hydrates [40], metals and their alloys [41–44]	Low- to high-temperature (approximately 10–800 °C)	High latent heat per volume, high thermal conductivity, non-flammable	Corrosive, prone to supercooling or phase separation, high cost	Industrial heat recovery, solar thermal systems, electronics cooling

MEPCM shell materials can always be fundamentally categorized into inorganic materials and organic materials. Organic shell materials have been broadly adopted owing to their well-established synthesis methods, excellent film-forming properties, and strong encapsulation capability for liquids. Commonly used organic shell materials include melamine-formaldehyde (MF) [54–56] and urea-formaldehyde (UF) resins [57,58], polyurethane (PU) [59–61], polymethyl methacrylate (PMMA) [31,62], and polystyrene (PS) [63–65], etc. Among them, MF resin is the most widely employed in MEPCM fabrication because of its favorable thermal stability, remarkable mechanical strength, and cost-effectiveness. However, organic polymer shells also present certain limitations, including poor thermal resistance, flammability, and relatively low thermal conductivity, which collectively constrain the performance of MEPCMs under high-temperature conditions. Typical inorganic shell materials for MEPCMs include calcium carbonate ($CaCO_3$) [29,66–68], silicon dioxide (SiO_2) [69–72], zinc tungstate ($ZnWO_4$) [73], and titanium dioxide (TiO_2) [74–76], etc. These inorganic shell materials possess advantages such as remarkable thermal conductivity, excellent mechanical strength, and non-flammability, which collectively enhance the MEPCMs' heat transfer efficiency and thermal stability. Such characteristics enhance safety and make them particularly suitable for applications requiring rapid thermal response. Nevertheless, inorganic shell materials also present certain limitations, most notably their poor gas barrier properties and lack of flexibility. These drawbacks may result in the development of microcracks within the shell during the phase transition of the core materials, consequently undermining the structural integrity and long-term cycling stability of MEPCMs. To address the limitations associated with single-shell materials, recent studies have progressively concentrated on creating hybrid shell structures that combine organic polymers with inorganic components [77,78]. Such hybrid shells combine the flexibility of organic materials with the high thermal conductivity and non-flammability of inorganic constituents, thereby enhancing the mechanical robust-

ness and thermal responsiveness of MEPCMs while also improving their heat resistance and structural stability.

Continuous advancements in microencapsulation technology have greatly improved the performance of MEPCMs. Their widespread adoption in energy management, building insulation, textiles, and electronic thermal regulation arises from their outstanding features—high energy storage density, isothermal operation, precise temperature control, and a large specific surface area [63,79–84]. As application scenarios continue to diversify, there is a growing demand for functionalized MEPCMs endowed with tailored properties to meet specific performance requirements. To impart additional functionalities to MEPCMs, researchers have explored various strategies, including embedding specific functional nanoparticles into either the core or the shell or utilizing functional materials as the shell structure [26,27,85,86]. These approaches have led to the development of MEPCMs with diverse capabilities such as photo-responsiveness, magnetic responsiveness, antibacterial activity, and self-healing, etc. While retaining excellent thermal regulation performance, these functionalized MEPCMs enable intelligent responses and coordinated control under complex and dynamic conditions, thereby significantly expanding their application potential. Functionalizing MEPCMs by harnessing light as a triggering stimulus or energy input has become a significant area of research, covering various applications such as photothermal conversion [87], photocatalysis [88], and photoluminescence [89]. Among them, photothermal conversion MEPCMs demonstrate the ability to directly harvest light energy and transduce it into storable thermal energy via photothermal conversion mechanisms, which renders them highly suitable for dual-purpose applications involving passive thermal regulation and efficient solar energy harvesting. This functionality is typically achieved by incorporating strong light-absorbing materials, such as conductive polymers, carbon black, metal oxide nanoparticles, or graphene, into the core or shell layers. These functional materials demonstrate strong absorption in the visible-to-near-infrared (vis-NIR) region, enabling efficient conversion of solar energy to thermal energy. Subsequently, the generated thermal energy undergoes rapid convection to the PCMs to trigger their phase transition and facilitate energy capture. In contrast, the realization of photocatalytic functionality in MEPCMs primarily depends on the incorporation of semiconductor materials with photocatalytic activity, such as nanoscale stannic oxide (SnO_2), cadmium sulfide (CdS), zinc oxide (ZnO), titanium dioxide (TiO_2), etc. Such photocatalytic MEPCMs not only enable TES but also utilize photogenerated charge carriers (electron–hole pairs) under light irradiation to degrade organic pollutants or drive photochemical reactions, thereby achieving a synergistic integration of TES with pollutant remediation or chemical energy conversion. This strategy effectively integrates solar energy storage with photocatalysis, offering a novel technological pathway for solar-to-chemical energy conversion under the framework of carbon neutrality goals. In addition, photoluminescent MEPCMs are constructed by doping or coating photoluminescent functional materials (like rare earth materials, organic luminophores, and quantum dots, etc.) that emit light upon excitation by specific wavelengths. These photoluminescent MEPCMs not only maintain effective TES capacity but also demonstrate extensive application prospects in areas like architectural aesthetics, smart sensing, and safety indicators.

3. Photothermal Conversion MEPCMs

Photothermal materials are capable of efficiently transforming solar energy into thermal energy via their intrinsic physical mechanisms, which typically involve non-radiative transitions, localized surface plasmon resonance (LSPR), or electron–phonon coupling [90]. Based on their composition and structural characteristics, typical photothermal materials can be categorized into carbon-based materials (including carbon black, graphene,

and carbon nanotubes, etc.) [91], metal-based materials (including nanoparticles of gold, silver, and platinum, etc.) [92], organic materials (such as indocyanine green, polypyrrole, and polyaniline, etc.) [93,94], and other photothermal agents [95]. Integrating photothermal materials with MEPCMs not only significantly enhances their TES efficiency and thermal conductivity but also imparts excellent photothermal conversion capability.

3.1. Carbon-Based Photothermal Materials Integrated with MEPCMs

Carbon-based photothermal materials possess broad-spectrum optical absorption characteristics, exhibiting particularly strong absorption in the vis-NIR region [96]. As a result, they have emerged as one of the most widely researched materials for photothermal conversion. Upon absorbing light energy, carbon-based materials undergo electronic excitation from the ground state to excited energy levels, followed by non-radiative relaxation dominated by electron–phonon coupling, which rapidly converts the excitation energy into lattice vibrations, thereby generating thermal energy [97–99]. This efficient photothermal conversion pathway enables carbon-based photothermal materials, when integrated with MEPCMs, to significantly enhance the photothermal response rate and solar energy utilization efficiency of the system. Representative carbon-based photothermal materials include carbon black (CB), graphene oxide (GO), reduced graphene oxide (rGO), and carbon nanotubes (CNTs), etc. Li et al. [100] successfully fabricated octadecane@TiO_2 MEPCMs with *n*-octadecane as the core and titanium dioxide (TiO_2) as the shell via a sol–gel method. The MEPCMs exhibited a uniform spherical morphology, achieving uniform particle diameters between 2 and 4 μm (Figure 1a), and they demonstrated excellent TES performance, with melting and solidifying enthalpies of 154.24 J/g and 154.26 J/g, respectively, and an encapsulation efficiency of 65.84%. Based on the synthesized MEPCMs, a CNT-enhanced suspension was further developed. As shown in Figure 1b, the suspension containing only MEPCMs changed into a transparent state because of gravity, while the MEPCMs/CNT composite suspension exhibited good dispersion stability after 7 days due to the interweaving of CNTs. In contrast to pure water, the specific heat and thermal conductivity of the MEPCMs/CNT composite suspension (0.2 wt% CNT) were about 43.57% and 34.48% higher than those of pure water, respectively. More importantly, the photothermal conversion efficiency of the MEPCMs/CNT composite suspensions achieved as high as 86.0 ± 1.5% in the simulated sunlight irradiation experiment with a light intensity of about 1 ± 0.03 W/cm^2 (Figure 1c), showing its significant potential for effectively capturing and storing solar energy.

In addition to simply compounding carbon-based materials with MEPCMs to make suspensions, they can also be introduced during the preparation of microcapsules to fabricate MEPCMs with high photothermal conversion capability. Chen et al. [101] designed a chitosan (CS)/carbon black (CB)-modified phase-change microcapsule (CB/CS-MePCM), employing titanium dioxide (TiO_2) as an inorganic shell, and encapsulating *n*-docosane as the PCM core, and they then further coated the surface of the microcapsules with a CB/CS composite layer to enhance the solar absorption efficiency. As shown in Figure 2a, TiO_2-MePCM exhibited a smooth surface and a regular spherical morphology. However, CB/CS-MePCM showed a coarser surface because of the presence of some CB and CS nanoparticles embedded on the surface, which suggested that a CB/CS nanocomposite layer was successfully decorated on TiO_2-MePCM. The differential scanning calorimetry (DSC) analysis demonstrated that CB/CS-MePCM still retained remarkable TES capacity (>140 J/g), even after undergoing layer-by-layer microencapsulation. Additionally, the leakage rate of CB/CS-MePCM was only 1.73% after heating for 12 h at 65 °C, which was lower than that of CS-MePCM (2.21%) and TiO_2-MePCM (3.25%), respectively, due to the layer-by-layer microencapsulation. The UV-vis-NIR spectroscopic analysis indicated

that the CB/CS-MePCM exhibited excellent light absorption capacity thanks to the reasonable combination of CB and CS (Figure 2b). CB/CS-MePCM achieved 95.04% light absorption efficiency, much higher than that of CS-MePCM (53.94%) and TiO_2-MePCM (41.60%), respectively. Yuan et al. [102] synthesized paraffin/nano-graphite (NG)@SiO_2 MEPCMs via in situ polycondensation of tetraethoxysilane (TEOS), forming a SiO_2 shell to achieve efficient encapsulation of both paraffin and NG. As shown in Figure 2c, compared with paraffin@SiO_2 MEPCMs, the addition of NG reduced the aggregation of SiO_2, resulting in paraffin/NG@SiO_2 MEPCMs with a more complete spherical morphology. The melting and solidification enthalpies of paraffin@SiO_2 MEPCMs were 91.9 J/g and 89.7 J/g, respectively, while the encapsulation efficiency was determined to be 52.7%. After the introduction of NG, the enthalpy value of paraffin/NG@SiO_2 MEPCMs decreased slightly, with the encapsulation efficiency dropping to 47.5% due to the partial replacement of paraffin. However, the introduction of NG also led to significant performance enhancements. On the one hand, NG enhanced the thermal conductivity of paraffin/NG@SiO_2 MEPCMs to 1.562 W m^{-1} K^{-1}, approximately 5 times that of pure paraffin (Figure 2d). On the other hand, the introduction of NG also enhanced the absorption capacity of MEPCMs for visible light. Compared with the paraffin@SiO_2 MEPCMs, the absorption of paraffin/NG@SiO_2 MEPCMs reached more than 70% (Figure 2e). Incorporating paraffin/NG@SiO_2 MEPCMs into water enhanced the water's thermal conductivity, heat capacity, and photothermal performance for solar receiver applications. Through boosting the efficiency of both heat transfer and light absorption, the composite fluid exhibits excellent solar energy capture and storage capabilities, which provides a new material design idea for the performance optimization of solar thermal utilization systems. In addition, Sun et al. [82] utilized graphene oxide (GO) and cellulose nanocrystal (CNC) to construct a stable Pickering emulsion for efficient encapsulation of octadecane (C18) and docosane (C22) through oxidative self-polymerization of dopamine and in situ polymerization MF resin. Polydopamine (PDA) not only had good photothermal conversion ability but also reduced GO to rGO, thereby elevating the solar-to-thermal conversion efficiency of the shell. C22@CNC/rGO/PDA/MF MEPCMs exhibited excellent TES performance and thermal cycling stability, with an encapsulation efficiency for C22 reaching 84.3% and a phase-change enthalpy of 175.4 J/g [82]. After 44 min of simulated light irradiation at 1 W/cm^2, the temperature of 15 wt% C22@CNC/rGO/PDA/MF MEPCMs slurry increased to 73 °C, higher than that of 15 wt% C22@CNC/GO/MF MEPCMs slurry (55 °C) without PDA and that of 15 wt% C22@CNC/PDA/MF MEPCMs slurry (65 °C) without GO, respectively, indicating a strong synergistic effect of rGO and PDA in boosting photothermal conversion efficiency [82].

3.2. Organic Photothermal Materials Integrated with MEPCMs

Organic photothermal materials typically exhibit high photo-absorption efficiency, photostability, and low preparation cost, establishing platform capabilities for solar–thermal energy harvesting. These materials absorb light energy of characteristic wavelengths through conjugated structures and subsequently transform the light energy into thermal energy via non-radiative transitions, thereby increasing the temperature of the materials [103,104]. Common organic photothermal materials mainly consist of organic small-molecule dyes such as diketopyrrolopyrrole (DPP), indocyanine green (ICG), Prussian blue (PB), etc., and conjugated polymers such as polyaniline (PANI), polydopamine (PDA), polypyrrole (PPY), etc. Yuan et al. [105] prepared PDA@MF/*n*-eicosane microencapsulated phase-change materials (PMPCMs) with a double-layer structure via a two-step in situ polymerization method, in which MF resin was utilized to encapsulate *n*-eicosane to form the inner shell of MPCMs, followed by self-polymerization of dopamine hydrochloride

to form a PDA outer shell. As shown in Figure 3a, both the single-layer MPCMs and the double-layer PMPCMs exhibited regular spherical shapes; in particular, the PMPCM-85 (with 85% *n*-eicosane) had a smoother and more uniform surface, indicating that the PDA layer helped enhance the morphological integrity [105]. PMPCM-85 had a significant phase-change enthalpy of 199.4 J/g and demonstrated excellent leakage resistance, with a leakage rate of only 2.6% after a 100 min leakage test at 80 °C (Figure 3b). Moreover, PDA, recognized as an effective photothermal material, significantly enhanced the photothermal conversion efficiency of PMPCMs. As shown in Figure 3c, under simulated solar irradiation, all PCPCM samples rapidly reached more than 80 °C within 160 s, which was much higher than that of the single-layer MPCM-85, which only reached about 34 °C. Similarly, Zhang et al. [106] initiated the polymerization of epoxy sodium p-styrenesulfonate and epoxy acrylate under ultraviolet lamp irradiation, encapsulating butyl stearate (BS) to obtain BS@PEA microcapsules featuring sulfonic acid groups on their surface. Subsequently, aniline was introduced and adhered to the surface of BS@PEA microcapsules through electrostatic interaction, followed by polymerization initiated by an ammonium persulfate aqueous solution. This process thus prepared double-shell multifunctional BS@PANI microcapsules for constructing anti-icing/de-icing composite coatings for all weather conditions [106]. As shown in Figure 3d, the surface of the microcapsules became progressively rougher with the rise in aniline concentration, thereby confirming the successful deposition and shell formation of PANI on BS@PEA microcapsules. The PANI not only improved the integrity of the shell but also imparted remarkable photothermal conversion capability, thermal conductivity, and anti-corrosion functionality. As shown in Figure 3e, compared to the uncoated surface, water droplets solidified approximately 12.6 times slower on the composite coating that included 10 wt% BS@PANI-3 microcapsules (incorporating 15 wt% aniline) on a chiller at –20 °C. Furthermore, under simulated near-infrared (NIR) irradiation (200 mW/cm^2), ice melting time required only 18 s on the composite coating, whereas the blank coating needed a nearly 10 times longer amount of time (Figure 3f). The introduction of PANI-based photothermal MEPCMs endowed the coating with excellent thermal regulation capability, opening new avenues for the fabrication of multifunctional anti-icing/de-icing coatings.

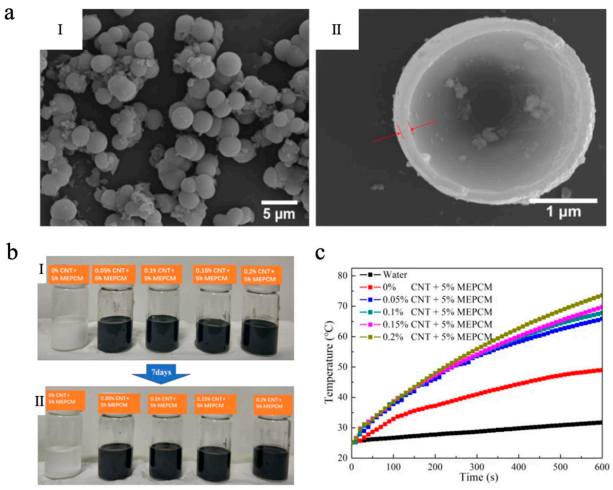


Figure 1. (**a**) SEM images of MEPCMs (I) and the microstructure of MEPCMs (II) [100]. Copyright © 2020, the authors [100] (licensed under: CC-BY 4.0). (**b**) Sedimentation photographs of the suspensions: 0 day (I) and 7 days (II) [100]. Copyright © 2020, the authors [100] (licensed under: CC-BY 4.0). (**c**) Temperature curves of water and mixed suspensions as a function of irradiation time [100]. Copyright © 2020, the authors [100] (licensed under: CC-BY 4.0).

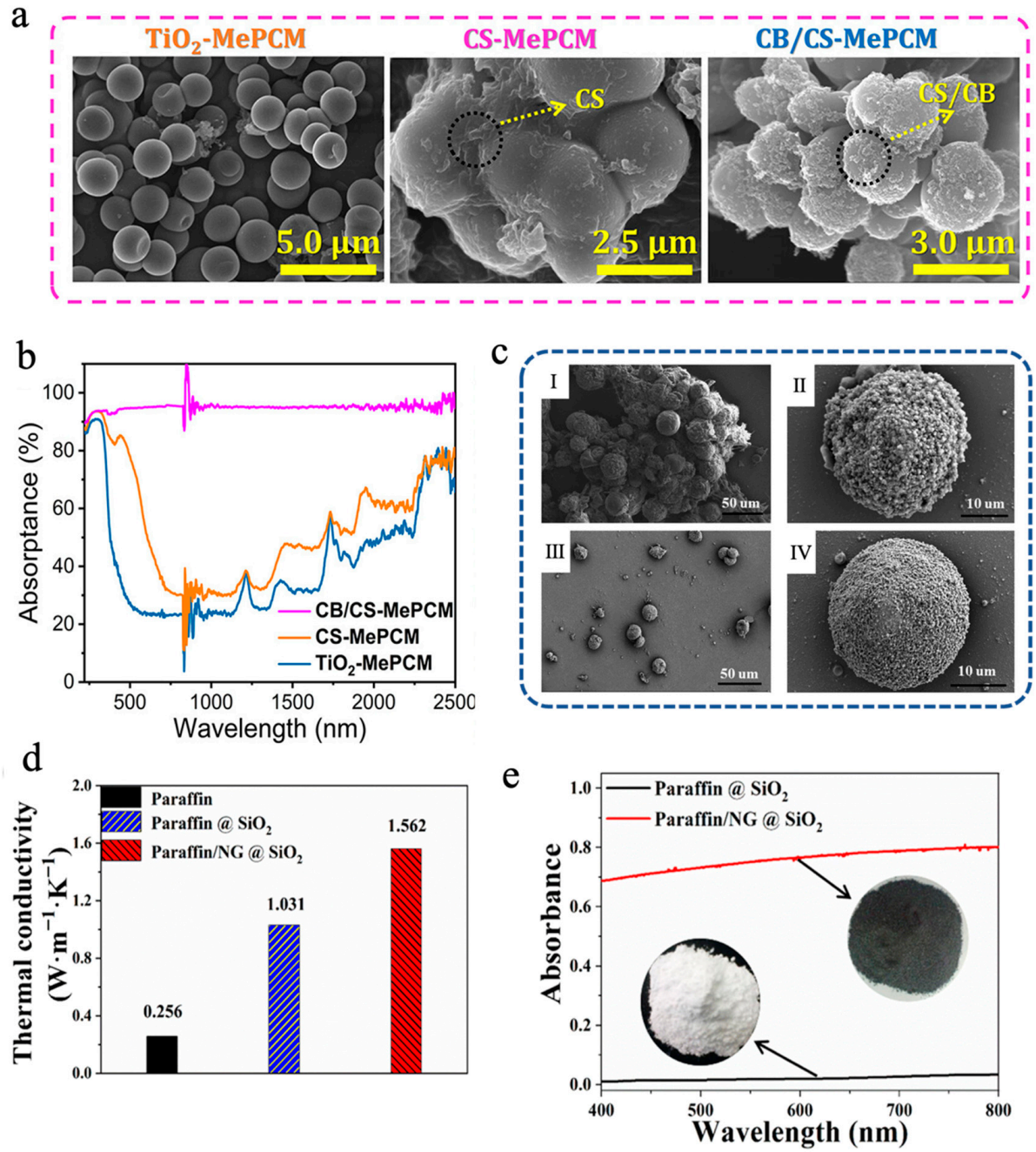


Figure 2. (**a**) SEM images of TiO_2-MePCM, CS-MePCM, and CB/CS-MePCM [101]. Copyright © 2023, American Chemical Society. (**b**) UV-vis-NIR absorption spectra of CB/CS-MePCM, CS-MePCM, and TiO_2-MePCM [101]. Copyright © 2023, American Chemical Society. (**c**) SEM images of paraffin@SiO_2 MEPCMs (I, II) and paraffin/NG@SiO_2 MEPCMs (III, IV) [102]. Copyright © 2024, Royal Society of Chemistry. (**d**) Thermal conductivities of paraffin/NG@SiO_2 MEPCMs, paraffin@SiO_2 MEPCMs, and pure paraffin solid powders [102]. Copyright © 2024, Royal Society of Chemistry. (**e**) UV-vis diffuse reflectance spectra of paraffin/NG@SiO_2 and paraffin@SiO_2 MEPCMs [102]. Copyright © 2024, Royal Society of Chemistry.

For the purpose of examining how various surfactants affect the polymerization process and the effectiveness of microcapsules, Li et al. [107] designed PPY-modified yeast phase-change microcapsules (PYPs) to boost the photothermal conversion efficiency and energy storage capacity of yeast phase-change microcapsules (YPs). Three surfactants with distinct hydrophilic and lipophilic balance (HLB) values—sodium dodecylbenzene sulfonate (SDBS), Span 80, and sodium dodecyl sulfate (SDS)—were used to systematically

analyze their effects on the synthesis of PPY. The results showed that when SDS was used as the surfactant with a 2:1 molar ratio to pyrrole, the PYPs (SDS) exhibited the best thermal conductivity and the lowest electrical resistivity (1.343 Ω·cm) [107]. This can be attributed to the high HLB of SDS, which facilitated small, stable micelles and a higher degree of polymerization, resulting in a dense and continuous PPY layer. Meanwhile, PYPs (SDS) demonstrated strong absorption of near-infrared light in the 400–1000 nm wavelength range, with a maximum absorbance of 1.19, whereas unmodified capric acid (CA)/lauric acid (LA) showed negligible light absorption in this spectral region. The incorporation of PPY significantly enhanced the photothermal conversion efficiency of CA/LA. In simulated light irradiation experiments, after 600 s of irradiation, PYPs (SDS) reached a maximum temperature of 35 °C, which was 7 °C higher than that of CA/LA [107].

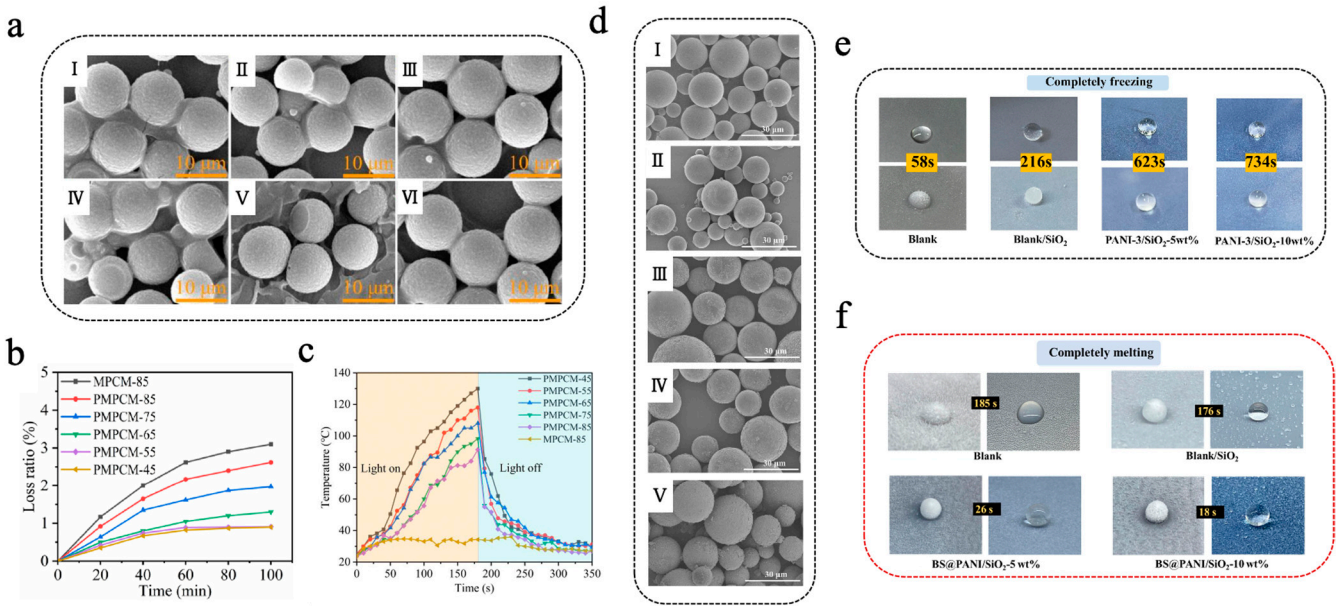


Figure 3. (**a**) SEM images of MPCM-45 (I), MPCM-65 (II), MPCM-85 (III), PMPCM-45 (IV), PMPCM-65 (V), and PMPCM-85 (VI) [105]. Copyright © 2021, Elsevier. (**b**) Loss ratio of MPCM-85 and PMPCMs for 100 min at 80 °C [105]. Copyright © 2021, Elsevier. (**c**) Temperature evolution curves of MPCM-85 and PMPCMs with light on/off [105]. Copyright © 2021, Elsevier. (**d**) SEM images of BS@PANI microcapsules with different aniline concentrations: BS@PEA (I), BS@PANI-1 (II), BS@PANI-2 (III), BS@PANI-3 (IV), and BS@PANI-4 (V) [106]. Copyright © 2024, Elsevier. (**e**) Images of freezing process of water droplets on various coated surfaces at −20 °C [106]. Copyright © 2024, Elsevier. (**f**) Images of melting process of ice on various surfaces when exposed to NIR light irradiation [106]. Copyright © 2024, Elsevier.

Beyond the single addition of organic photothermal materials, developing organic composite photothermal phase-change microcapsules can achieve more efficient photothermal conversion performance. Li et al. [108] prepared PDA and PPY composite photothermal phase-change microcapsules (SCN@PAP micro-PCMs), with *n*-octadecane (*n*-OD) as the core component and silicon dioxide (SiO_2) as the shell component, and they then deposited a PDA/PPY composite layer (PAP) on the surface to achieve efficient photothermal conversion. The findings indicated that incorporating PDA can enhance the optical performance of PPY. When the mass ratio of PY to DA was 1:0.032 and that of PAP to SCN micro-PCMs was 1:6, the SCN@PAP micro-PCMs exhibited the best light absorption performance and optimal morphology, achieving a photothermal conversion efficiency of 97.31%. The DSC results indicated that the SCN@PAP micro-PCMs displayed a melting enthalpy of 145.3 J/g, with an enthalpy loss of less than 1 J/g following 100 heating–cooling cycles, showcasing remarkable photothermal conversion efficiency and thermal storage stability.

3.3. Metal-Based Photothermal Materials Integrated with MEPCMs

Metal-based photothermal materials represent another category of efficient photothermal conversion materials, primarily operating through the LSPR effect, which exhibits significant light absorption in the vis-NIR regions. The LSPR effect is defined as the coherent oscillation of free electrons on metal nanoparticle surfaces excited by incident light at their resonant frequency, with subsequent conversion of light energy to heat through non-radiative decay mechanisms [109,110]. Meanwhile, the remarkable thermal conductivity of metal materials helps facilitate the rapid diffusion or directional accumulation of heat inside them, thereby further improving the photothermal conversion efficiency. Common metal-based photothermal materials mainly include nanoparticles of gold (Au), silver (Ag), and copper (Cu), etc. In MEPCM systems, the metal content typically ranges from trace amounts to several tens of weight percent, depending on the roles of the metal, such as functioning as a synergistic modifier and the primary photothermal component. Zhou et al. [111] successfully prepared silver nanoparticles (AgNPs)-modified microencapsulated phase-change materials (Ag@MPCM) and then integrated them into polyurethane acrylates (PUA) via UV curing. Through the LSPR effect, AgNPs enhanced both photothermal conversion and thermal conductivity of the Ag@MPCM. As shown in Figure 4a, with the increase in $AgNO_3$ added during the reaction, the surface of the microcapsules gradually became rougher, indicating the effective deposition of AgNPs onto MPCMs (0.75Ag@MPCM, 1Ag@MPCM, 1.5Ag@MPCM, and 2Ag@MPCM, representing $AgNO_3$-to-MPCM mass ratios of 0.75:1, 1:1, 1.5:1, and 2:1, respectively). Because AgNPs did not contribute to LHS during the phase-change temperature test, the encapsulation ratio (R) and efficiency of encapsulation (E) of Ag@MPCM gradually decreased with the increase in AgNPs, but the efficiency of TES (C) could still remain as high as 99% (Figure 4b) [111]. After 100 heating–cooling cycles, Ag@MPCM maintained stable thermal cycling performance, especially 1Ag@MPCM, with almost no enthalpy loss. In addition, owing to the high thermal conductivity of AgNPs, 1Ag@MPCM achieved a thermal conductivity of 0.643 W m^{-1} K^{-1}, 2.42 times that of the unmodified MPCM. Subsequently, MPCM and 1Ag@MPCM were integrated with flexible PUA resin to produce composite films. In comparison to pure PUA and 30MPCM-PUA (30 wt% MPCM in PUA), the 30Ag@MPCM-PUA sample (30 wt% 1Ag@MPCM in PUA) demonstrated a wider range of light absorption and higher absorption intensity throughout the spectrum (Figure 4c). During the simulated solar irradiation, 30MPCM-PUA showed a clear phase-transition plateau, while 30Ag@MPCM-PUA exhibited the fastest heating rate and reached the highest temperature. Furthermore, the temperatures of both 30Ag@MPCM-PUA and 30MPCM-PUA remained slightly elevated compared with PUA due to the thermal release from the PCM after the simulated light was turned off [111].

In more application scenarios, metal-based photothermal materials are often combined with other functional materials to achieve multifunctionality and synergistic enhancement. Peng et al. [112] developed an Au/TiO_2@PCM composite microcapsule, leveraging the LSPR effect of gold nanoparticles (AuNPs) to improve the visible light absorption of TiO_2, thereby enabling efficient photocatalytic hydrogen production and TES. AuNPs were loaded onto TiO_2 nanorods (TNR) and TiO_2 nanosheets (TNF) via a photodeposition method, yielding samples denoted as ATR and ATF, respectively. ATF@PCM and ATR@PCM were fabricated through the method of electrostatic self-assembly, with the detailed preparation procedure and microstructures illustrated in Figure 5a,b. After 15 min of simulated light irradiation, the temperatures of ATF@PCM and ATR@PCM reached 63.0 °C and 67.3 °C, respectively, both higher than that of unmodified Me-PCMs (Figure 5c). The thermal storage efficiency of ATR@PCM, ATF@PCM, and Me-PCM is shown in Figure 5d. During photothermal catalytic hydrogen production experiments, the light-

to-hydrogen (LTH) efficiency of ATF@PCM and ATR@PCM was 5.0‰ and 11.4‰, respectively, after 3 h of simulated light irradiation, representing 56.1% and 53.8% improvements compared with pure ATF and ATR without microencapsulation. Additionally, ATR@PCM exhibited superior performance in both photothermal conversion and photocatalytic hydrogen production compared with ATF@PCM, which was due to the larger specific surface area of ATR. Lou et al. [113] designed a synergistically enhanced multilayer melamine-formaldehyde resin@octadecane microcapsule (OMPA) integrated with PPY and silver nanoparticles (AgNPs) to improve photothermal conversion efficiency. Octadecane (OD) was used as the core PCM, which was initially encapsulated with an MF resin shell to obtain OM. Subsequently, a PPY layer was applied to the surface of OM through a simple oxidative self-polymerization process to obtain OMP. Finally, AgNPs were deposited onto the surface of OMP through chemical plating to construct a multifunctional composite shell. As shown in Figure 5e, SEM images revealed that a PPY layer improved the surface roughness of the microcapsules, which provided numerous attachment sites for AgNPs. As a result, the AgNPs loading of OMPA was significantly higher than that of OMA (without PPY modification). The DSC results revealed that the enthalpy of melting of OMPA was 101.3 J/g, indicating a high capacity for TES. After 100 heating–cooling cycles, neither the chemical structure nor the thermal properties of OMPA changed significantly, demonstrating excellent cycling stability. The synergistic effect of the LSPR effect of AgNPs and the conjugation effect of PPY significantly improved the photothermal conversion efficiency of OMPA. Additionally, the thermal conductivity of OMPA was boosted because of the electron transfer occurring between AgNPs and PPY. The photothermal energy storage conversion tests and the temperature change curves of OMPA, OMA, OM, and OD are shown in Figure 5f. Analysis indicated that the photothermal conversion efficiency of OMPA was 94.3%, surpassing those of OMP (83.6%) and OMA (88.2%). The thermal conductivity of OMPA attained a value of 1.0343 W m^{-1} K^{-1}, representing an increase of 374.2% compared to that of pure OD, thereby promoting the rapid storage of thermal energy converted from solar energy. Similarly, Zhang et al. [114] adhered PDA to the surface of paraffin@silicon dioxide (Pn@SiO_2) microcapsules via self-polymerization and then utilized the weak reducibility of PDA to reduce silver ammonia ions into AgNPs to form Pn@SiO_2@PDA/Ag microspheres. The Pn@SiO_2@PDA/Ag microcapsules had a phase-change enthalpy of more than 130 J/g and a high photothermal conversion efficiency of 88.7%.

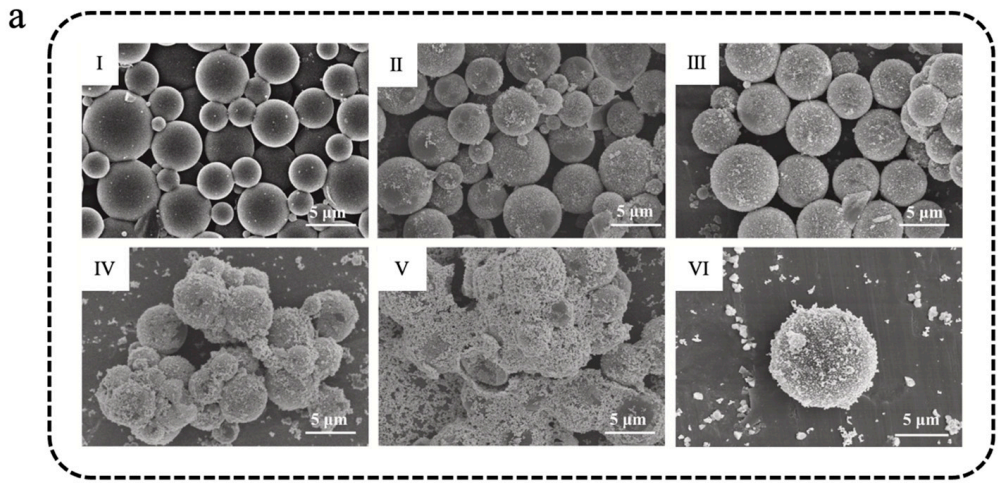


Figure 4. *Cont.*

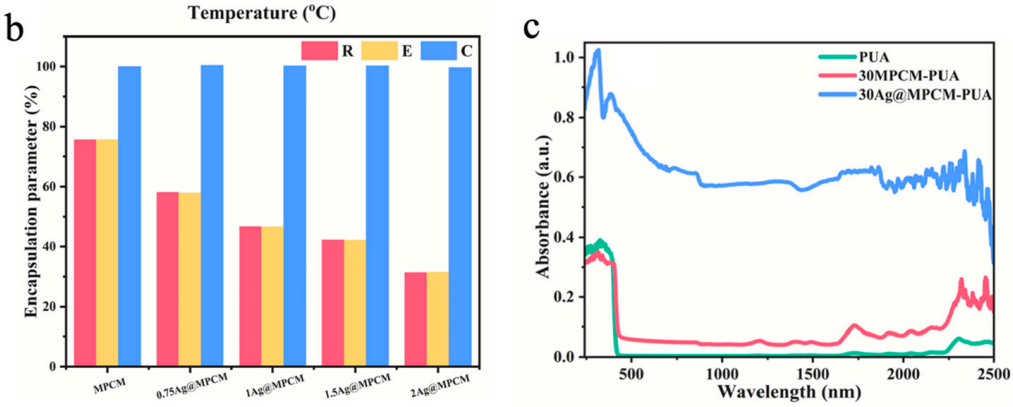


Figure 4. (**a**) SEM images of MPCM (I), 0.75Ag@MPCM (II), 1Ag@MPCM-85 (III,VI), 1.5Ag@MPCM (IV), and 2Ag@MPCM (V) [111]. Copyright © 2025, Elsevier. (**b**) The encapsulation ratio (R), efficiency of encapsulation (E), and efficiency of TES (C) of MPCM and Ag@MPCM [111]. Copyright © 2025, Elsevier. (**c**) Spectra of composite films in the UV-vis-NIR wavelength range [111]. Copyright © 2025, Elsevier.

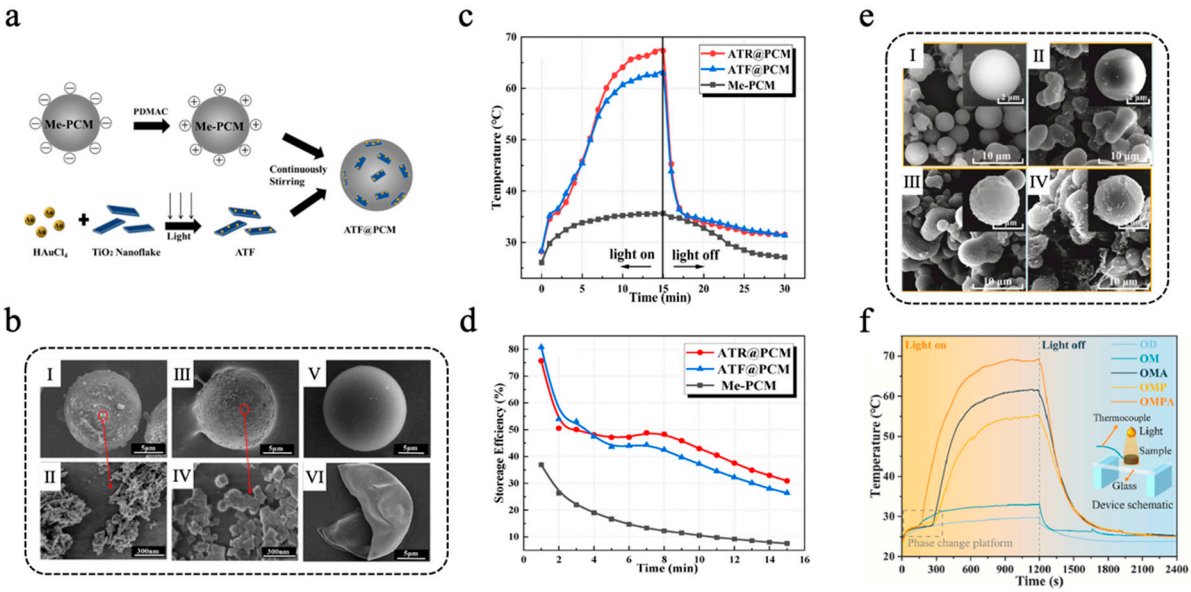


Figure 5. (**a**) Diagram of ATF and ATF@PCM preparation process [112]. Copyright © 2022, Elsevier. (**b**) SEM images of ATR@PCM: (I) overall morphology and (II) magnified view of the area indicated by the red circle, ATF@PCM: (III) overall morphology and (IV) magnified view of the area indicated by the red circle, intact Me-PCM (V), and broken Me-PCM (VI) [112]. Copyright © 2022, Elsevier. (**c**) Temperature–time curves of Me-PCM, ATF@PCM, and ATR@PCM [112]. Copyright © 2022, Elsevier. (**d**) The thermal storage efficiency of ATR@PCM, ATF@PCM, and Me-PCM [112]. Copyright © 2022, Elsevier. (**e**) SEM images of OM (I), OMA (II), OMP (III), and OMPA (IV) [113]. Copyright © 2025, Elsevier. (**f**) Diagrams of photothermal conversion experiment and temperature change curves of OMPA, OMA, OM, and OD [113]. Copyright © 2025, Elsevier.

3.4. Other Photothermal Materials Integrated with MEPCMs

In addition to the photothermal conversion materials mentioned above, MXene, as a popular material in recent years, has also been widely studied and applied. Naguib et al. [115] synthesized titanium carbide (Ti_3C_2) MXene by selectively etching the Al layer from Ti_3AlC_2 using hydrofluoric acid (HF) at room temperature, followed by sonication in methanol. MXene is a type of graphene-like two-dimensional (2D) transition metal carbide, nitride, or carbonitride, obtained by selectively etching the A layer from $M_{n+1}AX_n$ phases, where A is a weakly bonded group element, M represents an early transition metal

element, and X stands for carbon (C) or nitrogen (N) [116–118]. As a result of the LSPR effect, MXene demonstrates exceptional light absorption and photothermal conversion abilities within the vis-NIR spectra. Incorporating MXene into MEPCMs can endow the system with strong thermal storage capacity, high thermal conductivity, and remarkable photothermal conversion performance.

Zhao et al. [119] used Ti_3C_2 MXene nanosheets to modify phase-change microcapsules. The C_{18}@SDB/MXene consisted of styrene divinylbenzene (SDB) copolymer as the shell, *n*-octadecane as the core, and Ti_3C_2 MXene nanosheets were anchored onto the surface of microcapsules via hydrogen bonding interactions with the emulsifier polyvinylpyrrolidone (PVP) [119]. The images depicting the microstructure of six distinct types of microcapsules, each containing varying amounts of Ti_3C_2 MXene, are presented in Figure 6a. Compared with the C_{18}@SDB, some thin slices can be observed on the surface of C_{18}@SDB/MXene, suggesting that the SDB/MXene composite shell was successfully synthesized. When the Ti_3C_2 MXene content reached 0.67 wt% (C_{18}@SDB/MXene-10), the ability of the microcapsules to disperse had been substantially reduced, suggesting that further addition of Ti_3C_2 MXene was impractical. In simulated light irradiation experiments, the light absorption performance of C_{18}@SDB/MXene was significantly improved in the 200–800 nm solar spectrum compared to C_{18}@SDB (Figure 6b). As shown in Figure 6c, the photothermal conversion efficiency (γ) of microcapsules gradually increased with the increase in Ti_3C_2 MXene, and the γ value of the C_{18}@SDB/MXene-10 reached 85 $\pm$ 7%, representing a 240% enhancement compared to that of C_{18}@SDB. Similarly, Zhang et al. [120] constructed a multilayer phase-change microcapsule (MXene/SA/SiO_2-MEPCMs) for sustainable solar-driven seawater desalination. In this design, *n*-docosane was first encapsulated with a silica (SiO_2) shell to form SiO_2-MEPCMs. A sodium alginate (SA) coating was then introduced via a crosslinking reaction to form SA/SiO_2-MEPCMs. Finally, MXene nanosheets were anchored onto the surface through hydrogen bonding, resulting in the final MXene/SA/SiO_2-MEPCMs structure [120]. SEM images of the obtained MEPCMs are shown in Figure 6d. The surface of SA/SiO_2-MEPCMs was significantly rougher than that of SiO_2-MEPCMs. After MXene nanosheets modification, both MXene/SA/SiO_2-MEPCMs and MXene/SiO_2-MEPCMs exhibited a few thin slices, indicating the successful deposition of MXene. DSC results showed that MXene/SA/SiO_2-MEPCMs possessed high latent thermal capacity, with a crystallization enthalpy (ΔH_c) and a melting enthalpy (ΔH_m) of 151.7 J/g and 156.1 J/g, respectively. The encapsulation efficiency exceeded 60%, and the leakage rate after 24 h of heating was only 0.8 wt%. Thanks to the excellent photothermal conversion capabilities and light absorption in the vis-NIR regions, the light absorption efficiency of MXene/SA/SiO_2-MEPCMs reached as high as 97.2%, significantly higher than that of SiO_2-MEPCMs (6.4%) and SA/SiO_2-MEPCMs (77.7%). In solar-driven desalination experiments, MXene/SA/SiO_2-MEPCMs exhibited outstanding interfacial evaporation performance, achieving an evaporation rate of 2.11 kg m^{-2} h^{-1} (Figure 6e). Moreover, compared to MXene/SA/SiO_2-SPHERE (without PCM), the cumulative evaporation mass after five one-sun illumination and natural cooling cycles increased by 1.4 kg m^{-2}, enabling continuous seawater desalination under intermittent solar irradiation [120].

To create inorganic hydrated salt microcapsules that possess outstanding photothermal conversion efficiency and heat storage capacity, Lu et al. [121] designed and prepared composite phase-change microcapsules (MXene/MPCMs), in which $Na_2HPO_4 \cdot 12H_2O$ was employed as the phase-change core. The SiO_2 shell was formed via the hydrolysis of TEOS, and then Ti_3C_2 MXene was incorporated via high-speed stirring. The composite structure of MXene and SiO_2 significantly enhanced the photothermal responsiveness of MPCMs. In the simulated light irradiation experiment with an irradiance of 100 mW/cm^2, both MPCM-1 (prepared by the mixer) and MPCM-2 (prepared by shearing mechanism)

exhibited increased heating rates and elevated maximum temperatures with the addition of Ti_3C_2 MXene, especially MPCM-2 [121]. Meanwhile, the melting enthalpy of MPCM-1 and MPCM-2 was 169.62 J/g and 115.4 J/g, respectively, which highlights their promising application potential in solar energy harvesting and conversion systems [121].

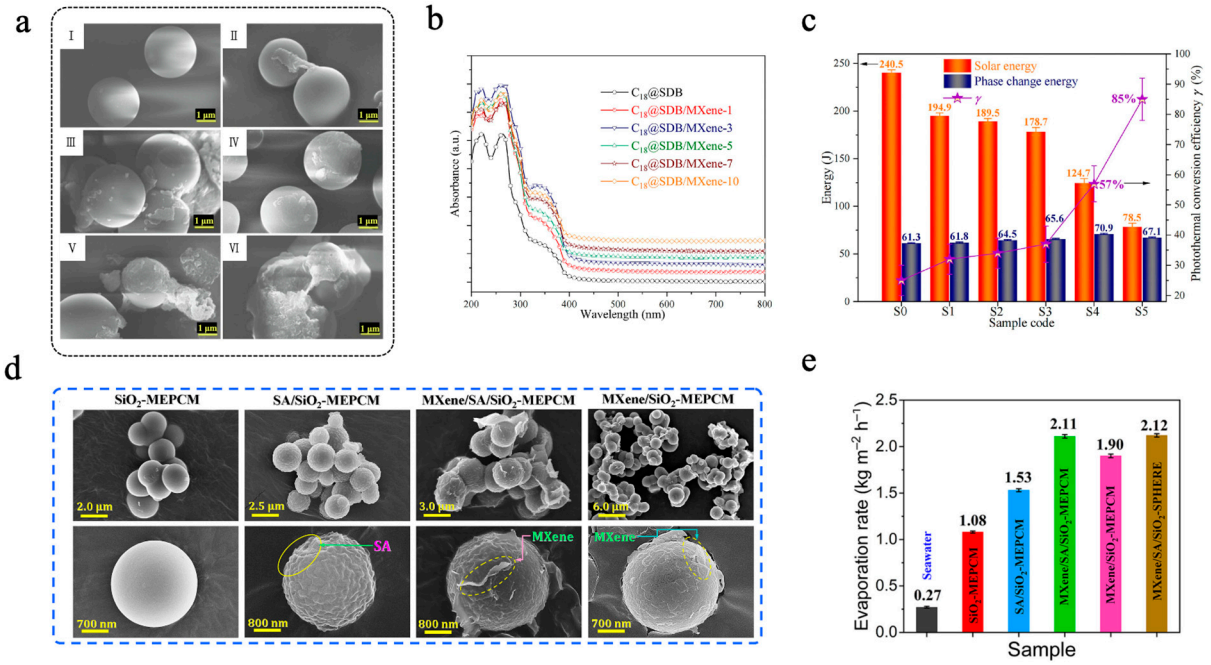


Figure 6. (**a**) SEM images of C_{18}@SDB (I), C_{18}@SDB/MXene-1 (II), C_{18}@SDB/MXene-3 (III), C_{18}@SDB/MXene-5 (IV), C_{18}@SDB/MXene-7 (V), and C_{18}@SDB/MXene-10 (VI) [119]. Copyright © 2023, Elsevier. (**b**) UV-vis-NIR absorption spectra [119]. Copyright © 2023, Elsevier. (**c**) Solar-to-heat conversion efficiency and energy storage performance of the microcapsules [119]. Copyright © 2023, Elsevier. (**d**) SEM images of SiO_2-MEPCMs, SA/SiO_2-MEPCMs, MXene/SA/SiO_2-MEPCMs, and MXene/SiO_2-MEPCMs [120]. Copyright © 2023, Elsevier. (**e**) Evaporation rates of seawater and evaporators based on microcapsule samples [120]. Copyright © 2023, Elsevier.

In summary, the incorporation of photothermal materials greatly enhances the solar absorption and thermal conductivity of MEPCMs, thereby improving their photothermal conversion efficiency. By converting absorbed solar energy into latent heat through the phase-change process, these MEPCMs achieve efficient energy capture and storage, expanding their potential in solar energy utilization and anti-icing applications.

However, carbon-based photothermal agents often suffer from poor dispersion and weak interfacial compatibility within the polymer matrix. These issues can lead to particle aggregation and reduced photothermal uniformity. Organic photothermal materials are susceptible to photodegradation and thermal instability under prolonged irradiation. Metallic photothermal additives provide excellent conductivity but are constrained by high cost, oxidation susceptibility, and relatively heavy density. Collectively, these drawbacks limit the long-term stability, cycling durability, and energy storage density of photothermal MEPCMs. Future research should therefore focus on improving the dispersion and interfacial bonding of carbon-based additives through surface modification or functionalized encapsulation techniques. It is also necessary to enhance the UV and oxidation resistance of organic and metallic photothermal agents via hybridization or coating strategies. Optimizing capsule architectures to balance photothermal efficiency and latent heat capacity will be equally important. In addition, more efforts are needed to develop cost-effective, environmentally friendly, and scalable synthesis methods to promote the industrial imple-

mentation of photothermal MEPCMs in real-world systems such as solar thermal storage, smart coatings, and thermal regulation textiles.

4. Photocatalytic MEPCMs

Photocatalytic materials represent a category of functional substances that can absorb solar energy and form electron–hole pairs to facilitate redox reactions. When the photon energy that photocatalytic materials absorb exceeds their bandgap energy, electrons (e^-) in the valence band (VB) are excited to the conduction band (CB), forming electron–hole pairs (e^-/h^+). Subsequently, the e^- and h^+ migrate to the semiconductor surface, where e^- can reduce acceptors and h^+ can oxidize donors. The resulting reactive oxygen species (ROS) can further degrade pollutants, split water for hydrogen production, or reduce CO_2, achieving the purpose of the photocatalytic reaction [85,88,122–124]. Common photocatalytic materials mainly include ZnO, TiO_2, Cu_2O, MoS_2, CdS, etc. The combination of photocatalytic materials with MEPCMs can achieve the synergistic optimization of light energy conversion, TES, and photocatalytic functions, enhancing light energy utilization efficiency while promoting the stability of photocatalytic reactions.

Due to its wide bandgap (~3.4 eV), nano-ZnO exhibits excellent photocatalytic activity in the ultraviolet (UV) region [122,123]. Chen et al. [124] fabricated PW@$CaCO_3$/ZnO microcapsules via an in situ polymerization method, which used paraffin wax (PW) as the core material, calcium carbonate ($CaCO_3$) as the shell material, and doped ZnO nanoparticles with different mass fractions (0.03–0.15 wt%) onto the surface of the shell to achieve dual applications of TES and photocatalytic degradation. As shown in Figure 7a, the DSC findings indicated that the phase-change enthalpy of PW@$CaCO_3$/ZnO microcapsules initially increased with the increase in ZnO addition, followed by a decrease possibly due to emulsion destabilization introduced by excess ZnO nanoparticles. Among all samples, PC-Z1 (with a ZnO content of 0.03 wt%) had the highest phase-change enthalpy, with a melting enthalpy of 93.1 J/g, which was significantly higher than that of PW@$CaCO_3$ (51.9 J/g).Concurrently, PW@$CaCO_3$/ZnO microcapsules exhibited remarkable thermal stability and high thermal conductivity during the phase-change process, and PC-Z5 (the content of ZnO was 0.15 wt%) achieved a maximum thermal conductivity of 1.268 W/(m·k), which was 150.1% higher than that of PW@$CaCO_3$ (Figure 7b). As shown in Figure 7c, UV-vis spectroscopy showed that the light absorption capacity of PW@$CaCO_3$/ZnO microcapsules was enhanced with the increase in ZnO content. The photocatalytic efficiency was evaluated by dispersing the microcapsules in a methylene blue (MB) dye solution. As shown in Figure 7d, the photocatalytic efficiency of MB under UV irradiation improved with the increase in ZnO content in the microcapsules. Among all samples, PC-Z5 had the highest photocatalytic efficiency, achieving a degradation rate of 98.97% after 12 h of UV irradiation. These results highlight the great potential of ZnO-modified microcapsules in TES and the mitigation of environmental pollution. As ZnO possesses a relatively wide bandgap (~3.4 eV), its photocatalytic response is mainly restricted to the UV region. To enhance visible-light activity, several modification strategies have been developed, including metal or non-metal doping (e.g., Ag, Mn, F, N, S) [125–128], construction of heterojunctions [129,130], or coupling carbon materials [131,132]. Yuan et al. [133] employed Ag to improve the visible-light absorption of ZnO by utilizing its plasmonic resonance effect and prepared CS/ZnO-Ag composite microcapsules (SCSM). Under xenon lamp irradiation, SCSM showed a much faster heating rate than microcapsules containing only Ag or ZnO, demonstrating a synergistic effect between the two components. The incorporation of Ag nanoparticles introduces impurity levels and localized surface plasmon resonance, which broaden the absorption range of ZnO from the UV to the visible region.

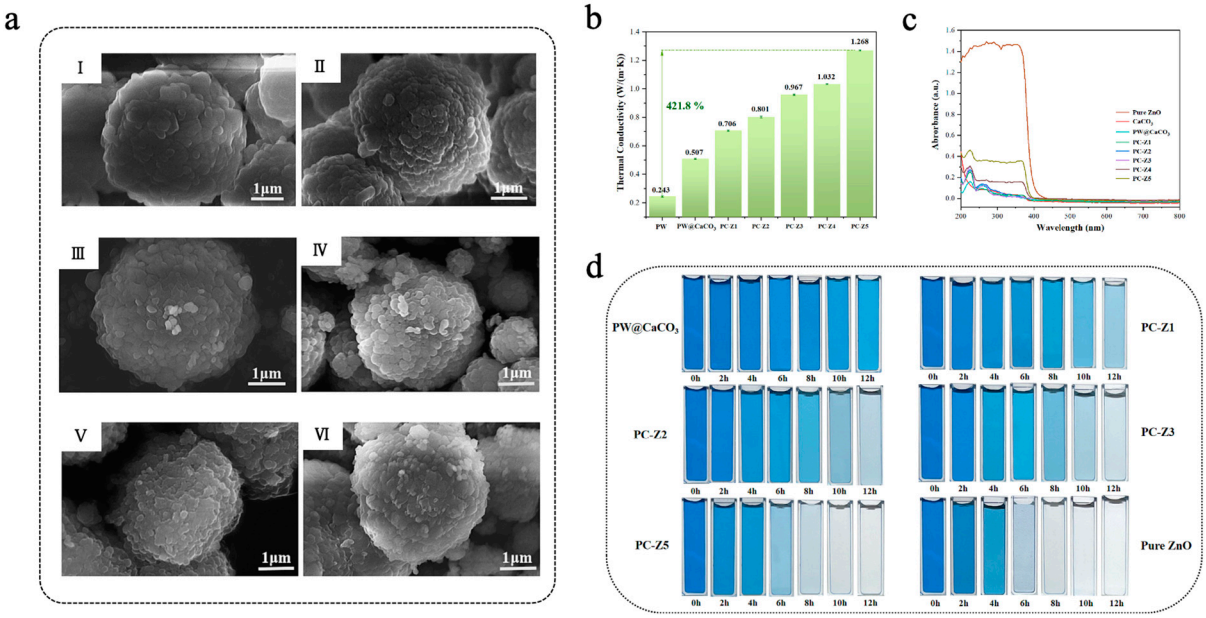


Figure 7. (**a**) SEM images of PW@$CaCO_3$ (I), PC-Z1 (II), PC-Z2 (III), PC-Z3 (IV), PC-Z4 (V), and PC-Z5 (VI) [124]. Copyright © 2024, Elsevier. (**b**) Thermal conductivity of pure ZnO, $CaCO_3$, PW@$CaCO_3$, PC-Z1, PC-Z2, PC-Z3, PC-Z4, and PC-Z5 [124]. Copyright © 2024, Elsevier. (**c**) UV-vis spectra of pure ZnO, $CaCO_3$, PW@$CaCO_3$, PC-Z1, PC-Z2, PC-Z3, PC-Z4, and PC-Z5 [124]. Copyright © 2024, Elsevier. (**d**) Digital images of photocatalytic degradation of MB dye solutions with various catalysts [124]. Copyright © 2024, Elsevier.

TiO_2, as one of the most representative photocatalytic materials, has been widely studied due to its low cost and high chemical stability [134,135]. Zhao et al. [136] prepared TiO_2-doped SDB copolymer microcapsules via suspension polymerization. To improve compatibility with the organic shell, TiO_2 nanoparticles were rendered amphiphilic by grafting with 3-glycidoxypropyltrimethoxysilane (KH560), thereby enhancing their anchoring ability at the oil–water interface. DSC results showed that sample S4 (doped with 4.0 wt% TiO_2) had the best TES performance among all modified samples, with microencapsulation efficiency (E_{en}) and heat storage efficiency (E_{es}) reaching 48.0 ± 0.4% and 47.7 ± 0.3%, respectively. However, when the doping rate of TiO_2 was increased to 5.0 wt% (sample S5), the TES performance dropped significantly, with E_{en} and E_{es} decreasing to 30.0 ± 0.7% and 29.8 ± 0.5%, respectively. This degradation may be attributed to excess TiO_2 nanoparticles disrupting emulsion stability, leading to microcapsule agglomeration and *n*-octadecane leakage. The photocatalytic performance was assessed through the degradation of methylene blue (MB) dye solution under UV irradiation. The degradation rate of MB by sample S4 was 90.92%, while that of sample S0 was only 6.2%. Even after five consecutive photocatalytic cycles, the degradation rate of sample S4 only decreased by 1.36%, indicating good thermal storage performance and efficient photocatalytic property. Similarly, Wang et al. [77] prepared TiO_2-hybridized phase-change microcapsules (T-MPCM) via a combined approach of solvent evaporation and electrostatic self-assembly using paraffin (PA) as the phase-change core and ethyl cellulose (EC) as the shell material. Due to the positively charged surface of TiO_2 nanoparticles and the negatively charged nature of EC, the TiO_2 nanoparticles were uniformly loaded onto the surface of microcapsules through electrostatic attraction without additional coupling agents. As shown in Figure 8a, the microcapsules exhibited good dispersibility and complete spherical structures. The introduction of TiO_2 nanoparticles increased surface roughness, and the cracked microcapsules also revealed the successful encapsulation of PA. The EDS diagram also identified the presence of Ti, confirming that the nanoparticles present on the microcapsule

surface were titanium dioxide. The photocatalytic performance was assessed through the degradation of MB solution under UV-light irradiation. As shown in Figure 8b, the absorbance of MB at 616 nm and 665 nm gradually decreased with prolonged UV irradiation. After 200 min, the MB solution became nearly transparent, with a degradation rate of 91.9%. Even after five consecutive photocatalytic cycles, the degradation rate decreased by only 2.5%, demonstrating excellent photocatalytic performance and good cycling stability. Subsequently, the microcapsules were combined with waterborne acrylic emulsion with varying dosages to prepare composite coatings with photocatalytic functions. As shown in Figure 8c, coatings incorporating T-MPCMs exhibited stronger MB degradation under UV light compared to the MPCM coating, with the photocatalytic effect intensifying as the T-MPCM content increased.

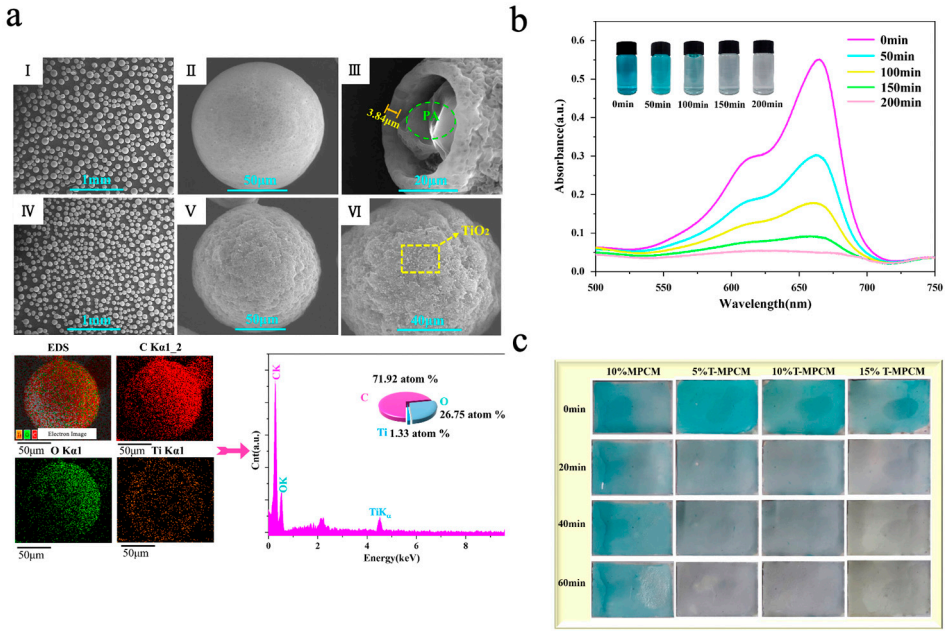


Figure 8. (**a**) SEM images of MPCM (I–III) and T-MPCM (IV–VI) and EDS image of T-MPCM [77]. Copyright © 2024, Elsevier. (**b**) UV-vis spectra of and photos of MB solution [77]. Copyright © 2024, Elsevier. (**c**) Photos of the coatings under UV irradiation [77]. Copyright © 2024, Elsevier.

For the purpose of further enhancing the photocatalytic activity of TiO_2, Zhao et al. [137] developed multifunctional fluorine-doped TiO_2 phase-change material microcapsules. The introduction of F effectively modulated the band structure of TiO_2 nanoparticles, broadened their light absorption range, and consequently improved the photocatalytic performance of the microcapsules. The photoluminescence (PL) test results showed that the TiO_2 nanoparticles exhibited a strong luminescence peak at 390 nm, while the F-doped TiO_2 PCM microcapsules had almost no luminescence response in this range, indicating that F doping significantly suppressed the radiative recombination process between photogenerated electrons and holes in TiO_2 nanoparticles, thereby enhancing their photocatalytic efficiency. The photocatalytic performance was assessed via the visible-light-driven degradation of Rhodamine B (RhB) solution (0.025 g/L). The results showed that F-doped TiO_2 PCM microcapsules exhibited a significantly higher degradation rate than TiO_2 nanoparticles throughout the illumination period, achieving complete degradation of RhB within 7 h. In addition, the particle size of the microcapsules had a significant effect on their photocatalytic performance. F-doped TiO_2 PCM microcapsules with a small diameter (100 μm) exhibited a higher specific surface area and greater adsorption capacity, and their reaction constant was seven times greater than that of microcapsules with a diameter of 300 μm, reflecting the important role of size regulation in improving catalytic efficiency.

In addition to the common photocatalytic materials, FeOOH has also been widely studied in recent years as a visible-light-driven photocatalytic material with a wide bandgap and broad photo-response region [138,139]. Xu et al. [140] developed a novel phase-change microcapsule (paraffin@SiO_2/FeOOH) with SiO_2/FeOOH as a double-layer shell, which integrated both TES and photocatalytic degradation functionalities. Firstly, paraffin@SiO_2 microcapsules were constructed by interfacial polymerization, and then the negative charge of the SiO_2 shell under alkaline conditions was used to attract Fe^{2+} to aggregate and generate FeOOH on its surface in situ, finally obtaining paraffin@SiO_2/FeOOH microcapsules [140]. SEM and TEM images revealed that the paraffin@SiO_2 microcapsules exhibited uniform, smooth, and compact spherical structures, while paraffin@SiO_2/FeOOH microcapsules had rough flake structures on the surface, proving the successful deposition of FeOOH. DSC findings indicated that the melting and freezing enthalpy of paraffin@SiO_2/FeOOH microcapsules were 104.44 J/g and 101.69 J/g, respectively, with a paraffin encapsulation efficiency of 49.68%, demonstrating good latent heat storage capability. The photocatalytic performance of the microcapsules was evaluated by monitoring the degradation rate of MB solution under natural light. The paraffin@SiO_2/FeOOH microcapsules achieved a degradation efficiency of 80% within 2 h and reached 94% after 4 h. In cyclic photocatalytic tests, the microcapsules retained stable catalytic activity after five cycles. However, a notable decline in degradation efficiency was observed after ten cycles, which was mainly attributed to partial corrosion and deactivation of FeOOH on the shell. Therefore, the FeOOH-modified microcapsules have good photocatalytic ability, but their long-term stability still requires further improvement.

Moreover, emerging photocatalytic materials, such as perovskites [141–144], graphitic carbon nitride (g-C_3N_4) [145,146], and covalent organic frameworks (COFs) [147–149], possess broad light absorption ranges, high charge carrier mobility, large specific surface areas, and tunable band structures, demonstrating significant potential in photocatalysis and solar energy utilization. However, integrating these materials with MEPCM systems faces multiple challenges. Key obstacles include intrinsic stability issues (e.g., halide perovskites degrading under water, heat, or light), complex synthesis procedures incompatible with microencapsulation, and mismatches between optoelectronic properties and the thermal–physical requirements of MEPCMs systems. Additional challenges include interfacial side reactions, structural degradation during long-term cycling, localized overheating causing damage to encapsulation materials, high costs limiting scalability, and inefficient energy transfer pathways resulting in suboptimal photothermal conversion efficiency. Addressing these challenges requires careful material modification, composite structure design, and interfacial engineering.

In short, the incorporation of materials with photocatalytic properties (such as ZnO, TiO_2, etc.) into MEPCMs not only endows them with the capability to drive catalytic reactions under light irradiation but also achieves the synergistic function of TES and photocatalysis. Photocatalytic MEPCMs demonstrate broad application prospects in fields such as organic pollution degradation and solar-driven hydrogen production.

However, several challenges remain. Most photocatalytic fillers exhibit poor interfacial compatibility and uneven dispersion within the capsule matrix, which may reduce light utilization and catalytic efficiency. In addition, the photocatalytic activity of semiconductor materials often decreases after long-term irradiation due to particle agglomeration or photocorrosion. The relatively high loading of photocatalysts required to achieve strong catalytic effects can also compromise the latent heat capacity of the MEPCM system. Future research should focus on improving the interfacial bonding and dispersion of photocatalysts through surface functionalization or core–shell structural design. Enhancing the stability of semiconductor photocatalysts by doping, heterojunction engineering, or coating

strategies is also essential. Furthermore, more attention should be given to developing cost-effective, environmentally friendly, and scalable fabrication methods to promote the practical deployment of photocatalytic MEPCMs in environmental purification and solar-fuel generation systems.

5. Photoluminescence MEPCMs

Fluorescence is a typical photoluminescence phenomenon, essentially a non-thermal radiation (cold emission) process [150]. When fluorescence materials are excited by an external light source (such as ultraviolet or visible light), the energy provided by the photons promotes electrons from the lowest energy state to higher energy levels, such as the first or second excited states. Nevertheless, these excited states exhibit instability, causing the electrons to swiftly revert to the ground state via radiative transitions, releasing excess energy in the form of light and thus generating fluorescence [151,152]. Common fluorescent materials include inorganic fluorescent materials (rare earth materials, carbon quantum dots, etc.) and organic fluorescent materials (coumarin, polymer materials, and small-molecule materials, etc.). By incorporating fluorescent materials into the shell or core of MEPCMs, photoluminescence MEPCMs with both fluorescent properties and thermal storage capabilities can be fabricated.

Inorganic fluorescent materials such as calcium tungstate ($CaWO_4$), zinc tungstate ($ZnWO_4$), and copper tungstate ($CuWO_4$) exhibit excellent photoluminescence properties due to their unique WO_4^{2-} tetrahedral structure [153]. Liu et al. [154] prepared multifunctional phase-change microcapsules (PW@$CaWO_4$) via an in situ polymerization method using inorganic $CaWO_4$ as the shell material and paraffin wax (PW) as the phase-change core. The impact of two distinct emulsifiers, namely, a cationic surfactant, cetyl trimethyl ammonium bromide (CTAB), and an anionic surfactant, sodium dodecyl-benzenesulfonate (SDBS), on the morphology and performance of the MEPCMs was systematically studied. As shown in Figure 9a, the O^{2-} in the hydrophilic group of SDBS formed a covalent bond with Ca^{2+}, followed by the reaction of WO_4^{2-} with Ca^{2+} to generate the $CaWO_4$ shell. In contrast, the N^+ groups in the hydrophilic group of CTAB formed a covalent bond with WO_4^{2-}, followed by the reaction of Ca^{2+} with WO_4^{2-} to generate the $CaWO_4$ shell. SEM images revealed that the sample with SDBS as the emulsifier and a 1:1 core-to-shell ratio (PC-S2) exhibited the optimal spherical morphology, as the opposite charge of SDBS to Ca^{2+} facilitated uniform $CaWO_4$ deposition on the PW surface. Because of the $CaWO_4$ shell, the PW@$CaWO_4$ microcapsules had good thermal conductivity, with a minimum supercooling degree of 1.00 ± 0.08 °C, 3.41 °C lower than that of PW. UV-vis spectroscopy revealed that microcapsules prepared with CTAB (PC-C1/2/3) exhibited stronger UV absorption, accompanied via a minor blue shift in the absorption spectrum due to enhanced oxidation capacity of O^{2-} caused by WO_4^{2-} attraction to cationic emulsifiers (Figure 9b). As shown in Figure 9c, owing to high sphericity and good encapsulation, the microcapsules prepared with SDBS (PC-S1/2/3) displayed stronger overall fluorescence intensity than those prepared with CTAB (PC-C1/2/3). Furthermore, as the $CaWO_4$ shell content increased, fluorescence emission was significantly enhanced and gradually shifted to green, which was attributed to the quantum size effect of the $CaWO_4$ shell. Cheng et al. [73] synthesized phase-change microcapsules (NePCMs) with high thermal conductivity, latent heat values, and stability by using zinc tungstate ($ZnWO_4$) as the shell material to encapsulate stearic acid (SA) via in situ polymerization. When SDBS was used as the emulsifier and the core-to-shell ratio was 1:1, the NePCMs exhibited uniform and regular spherical morphology, along with the highest phase-change enthalpy of 83.63 J/g. In UV absorption and photoluminescence spectroscopy measurements, NePCMs demonstrated favorable UV absorption capacity and photoluminescent properties. Additionally, the preparation

of $ZnWO_4$ via this method can reduce the cost by 40%, showing outstanding potential in coating, fluorescent architecture, and textile industries.

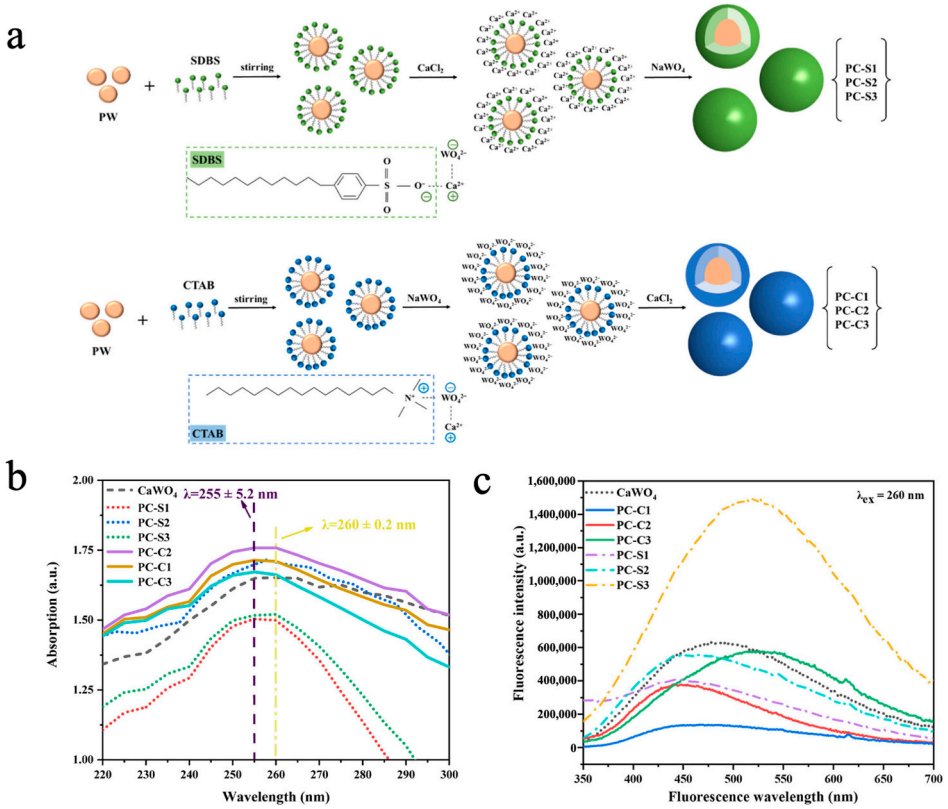


Figure 9. (**a**) Diagram of the PW@$CaWO_4$ microcapsules synthesis process [154]. Copyright © 2023, American Chemical Society. (**b**) UV absorption spectra of the PW@$CaWO_4$ microcapsules and the $CaWO_4$ [154]. Copyright © 2023, American Chemical Society. (**c**) Fluorescence spectra of the PW@$CaWO_4$ microcapsules and the $CaWO_4$ [154]. Copyright © 2023, American Chemical Society.

In addition, the incorporation of rare earth elements such as ytterbium (Yb) [155], cerium (Ce) [156], europium (Eu) [157], etc., can also endow phase-change microcapsules with desirable photoluminescent properties. Liu et al. [157] fabricated a europium-doped photoluminescent phase-change microcapsule (MePCM-Eu) via a Pickering emulsion templating method, which consisted of *n*-docosane as the core and a $CaCO_3/Fe_3O_4$ composite as the shell. $CaCO_3$ was used as the inorganic shell material due to its low cost, excellent thermal stability, and support for fluorescence emission, while the introduction of Eu^{3+} ions significantly enhanced the luminescence intensity. Fe_3O_4 nanoparticles, serving as both emulsion stabilizers and photothermal agents, not only improved the solar–thermal conversion efficiency but also reinforced the structural stability of the shell. As shown in Figure 10a, with increasing Eu^{3+} doping concentration, the surface of the microcapsules gradually became rough, but they still maintained a regular, compact core–shell spherical morphology, indicating good encapsulation integrity. Meanwhile, all MePCM-Eu samples exhibited phase-change enthalpies exceeding 125 J/g, demonstrating outstanding TES capability. The thermal responsiveness and thermal conductivity of MePCM-Eu-2 (doped with 0.134 g of $Eu(NO_3)_3 \cdot 6H_2O$) were improved thanks to the addition of Fe_3O_4 nanoparticles, which had good photothermal conversion capacity and high thermal conductivity. Photoluminescence measurements showed that MePCM-Eu exhibited Eu^{3+} emission peaks at 468, 589, 616, 702, and 765 nm under 394 nm excitation, while no significant emission was observed in MePCM (without Eu^{3+} doping), confirming that Eu^{3+} doping markedly enhanced luminescence intensity (Figure 10b). In the application test, MePCM-Eu-2 was

loaded onto polyester fabric and cut into the shape of 'BUCT' and finally adhered to a white coat. As shown in Figure 10c, it effectively absorbed and stored solar thermal energy during sunlight irradiation and gradually released heat at natural cooling to improve physiological comfort. When under UV illumination, the coating displayed a distinct red fluorescent pattern, indicating potential for visual recognition and smart textile applications.

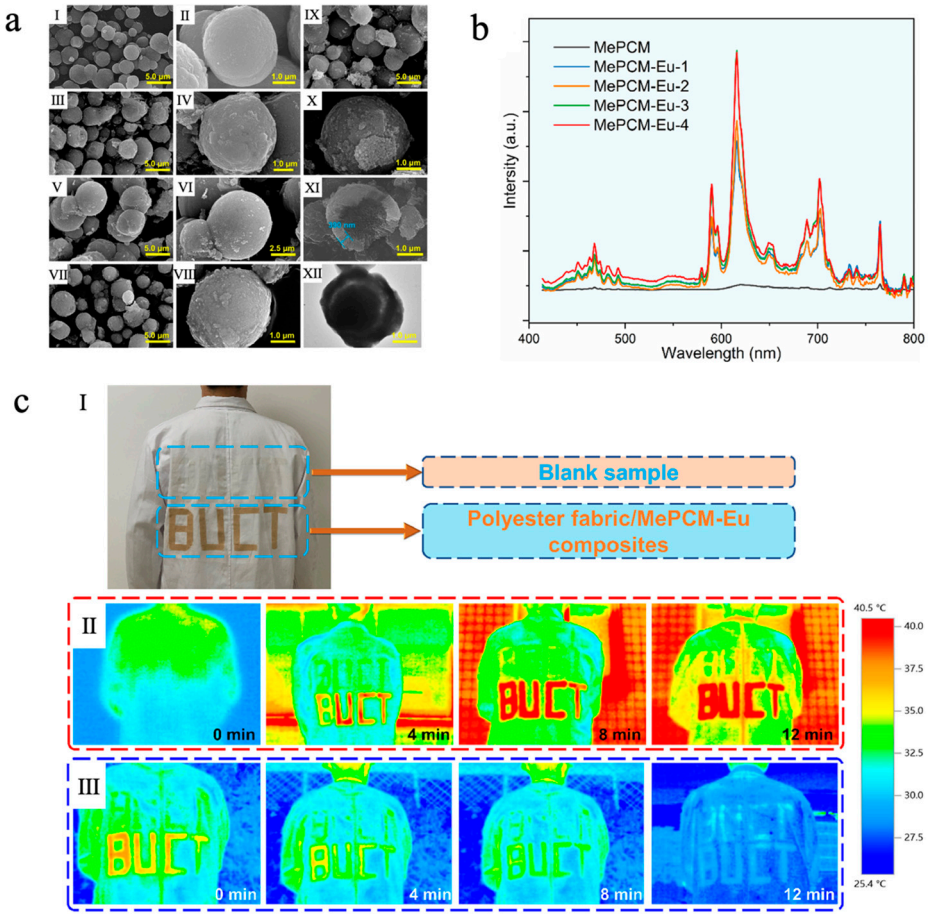


Figure 10. (**a**) SEM images of MePCM (I, II), MePCM-Eu-1 (III, IV), MePCM-Eu-2 (V, VI), MePCM-Eu-3 (VII, VIII), and MePCM-Eu-4 (IX–XI); TEM image of MePCM-Eu-4 (XII) [157]. Copyright © 2022, Elsevier. (**b**) Emission spectra of MePCM-Eu with varying Eu^{3+} doping concentrations under an excitation wavelength of 394 nm [157]. Copyright © 2022, Elsevier. (**c**) An image of a subject wearing a white coat coated with the polyester fabric/MePCM-Eu-2 composite bearing a 'BUCT' design, accompanied by pristine polyester fabric as a blank sample (I), infrared thermal images of the white coat captured outdoors under varying solar irradiation durations (II), and those captured indoors under varying natural cooling durations (III) [157]. Copyright © 2022, Elsevier.

With the deepening research fluorescence regulation mechanisms, the fluorescence phenomenon not only depends on the energy level structure of molecules but is also significantly influenced by their aggregation state and the surrounding environment. Traditional luminescent molecules typically exhibit efficient fluorescence in dilute solutions; however, their fluorescence intensity is often weakened or even completely quenched in concentrated solutions or aggregated states. This phenomenon is known as aggregation-caused quenching (ACQ). By leveraging this phenomenon, integrating luminescent molecules with MEPCMs can achieve not only TES and temperature regulation but also reversible regulation of fluorescence [158,159]. Yu et al. [160] designed a fluorescence sensing system (MIP@CQD-PCM) by integrating molecularly imprinted MEPCMs with carbon quantum dots (CQDs) for the efficient detection and recognition of tetracycline. As shown in

Figure 11a, in this system, *n*-eicosane served as the phase-change material core, while CQDs were embedded within a SiO_2 shell. The SiO_2 shell surface was coated with a tetracycline-templated molecularly imprinted polymer (MIP) layer, after which the tetracycline template was eluted from the MIP layer. By combining the molecular imprinting technique with specific recognition sites and the fluorescent properties of CQDs, the system exhibited high adsorption of tetracycline with a fluorescence quenching response via ACQ. The MIP@CQD-PCM exhibited excellent TES capacity and stable phase transition cycling behavior, with an E_{en} of 77.11% and an E_{es} of 76.74%, which enhanced the accuracy and efficiency of tetracycline detection under high-temperature conditions. Furthermore, as shown in Figure 11b, the system exhibited a clear linear relationship between tetracycline concentration and fluorescence quenching intensity, in contrast to NIP@CQD-PCM without an MIP template. Due to the PCM core, the system showed better temperature-controlled fluorescence recognition performance compared to MIP@CQD-SPR without *n*-eicosane in high-temperature environments.

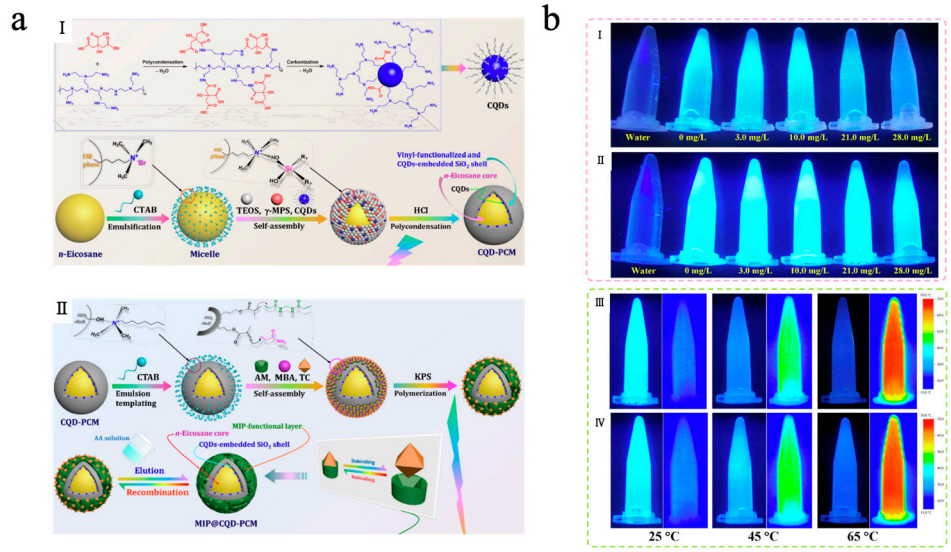


Figure 11. (**a**) Schematic of CQDs and CQD-PCM synthesis (I); schematic of MIP@CQD-PCM synthesis (II) [160]. Copyright © 2021, Elsevier. (**b**) Digital images of MIP@CQD-PCM (I) and NIP@CQD-PCM (II) suspensions under 365 nm UV irradiation at varying tetracycline concentrations. Digital images (**left**) and infrared thermograms (**right**) of MIP@CQD-PCM (III) and MIP@CQD-SPR (IV) suspensions under 365 nm UV irradiation at different equilibrium temperatures [160]. Copyright © 2021, Elsevier.

Therefore, the introduction of luminescent materials, such as rare earth materials, inorganic fluorescent materials, or CQDs, enables the fabrication of MEPCMs with both TES and photoluminescence functions. Fluorescent MEPCMs not only exhibit excellent thermal response characteristics but also generate stable fluorescence under specific wavelength excitation, expanding the application prospects in fields such as fluorescent architecture, smart coatings, and environmental detection.

However, some challenges remain to be addressed. The luminescence intensity of rare earth and fluorescent materials can be significantly affected by the thermal cycling process, leading to gradual fluorescence attenuation. In addition, the compatibility between luminescent fillers and the polymer shell is often limited, which may result in aggregation or fluorescence quenching. The relatively complex synthesis routes and high cost of rare earth materials also hinder their large-scale application. Future research should therefore focus on improving the interfacial stability between luminescent fillers and the encapsulation matrix, as well as enhancing the photostability of fluorescent agents under

repeated heating and cooling cycles. Developing low-cost, high-efficiency luminescent alternatives—such as surface-functionalized CQDs or hybrid nanostructures—could further improve performance. Moreover, efforts should be directed toward establishing scalable and environmentally sustainable synthesis techniques to promote the integration of luminescent MEPCMs into practical applications, including building illumination, smart coatings, and environmental monitoring.

6. Conclusions and Outlook

In summary, this article systematically reviews the recent research progress in photo-responsive MEPCMs, with a focus on the integration and performance optimization of three major types of functional materials: photothermal conversion, photocatalysis, and photoluminescence. The incorporation of photothermal materials significantly enhances the solar absorption capacity and thermal conductivity of MEPCMs, enabling efficient solar-to-thermal energy conversion and storage. The integration of photocatalytic materials allows MEPCMs to drive chemical reactions under light irradiation, allowing for the simultaneous realization of TES alongside functions like organic pollutant degradation and solar-driven hydrogen production. The introduction of luminescent components, such as rare earth materials, inorganic fluorescent materials, or carbon quantum dots, imparts stable photoluminescent properties to MEPCMs, thereby promoting the applications of MEPCMs in fluorescent architecture, smart coatings, and environmental sensing.

Despite significant progress in the development of photo-responsive MEPCMs, several key challenges remain to be addressed:

1. Trade-off between functional material loading and energy storage performance. Although photo-responsive components enhance light responsiveness, they do not directly contribute to the phase-change process. Excessive loading will significantly reduce the overall energy storage density.
2. High cost and complex fabrication processes. Most photo-responsive materials currently employed are expensive and require delicate synthesis and surface modification steps, making large-scale preparation of stable microcapsules technically demanding. As a result, most studies remain at the laboratory or proof-of-concept stage.
3. Interfacial compatibility among components. The mismatch between the core–shell structure and photo-responsive fillers can lead to leakage or degradation during thermal cycling. Improving interfacial bonding via surface modification, coupling agents, or gradient-interface engineering will enhance durability.
4. Limited multifunctional integration. Current studies primarily focus on the development of single- or dual-function MEPCMs. Future research should aim to achieve three or more functional properties by incorporating multiple types of functional materials.
5. Scalability and practical implementation. The industrial deployment of photo-responsive MEPCMs still faces challenges in terms of large-scale synthesis, process costs, and long-term reliability. Simplifying fabrication routes, improving encapsulation efficiency, and adopting environmentally sustainable methods will be essential to enable scalable production and real-world integration.

Looking forward, among the photo-responsive MEPCMs systems discussed, carbon-based photothermal MEPCMs currently exhibit the most promising potential for near-term industrial applications due to their mature synthesis routes, superior photothermal conversion efficiency, high stability, and relatively low cost. In contrast, photocatalytic MEPCMs are still largely limited to ultraviolet-light responsiveness, and their overall energy conversion efficiency remains modest. Emerging photocatalytic materials, such as perovskites and covalent organic frameworks (COFs), show excellent light absorption and charge transfer

characteristics. However, their integration with MEPCMs has been rarely explored, and systematic investigations on such composites remain scarce. Photoluminescent MEPCMs, on the other hand, are still in their early exploratory stage, mainly constrained by high material costs and relatively narrow application domains.

Future progress toward commercialization and large-scale implementation of photoresponsive MEPCMs will rely on addressing several critical challenges, including process scalability, long-term interfacial stability, and cycling durability of both materials and structures. Building sustainable and reproducible fabrication frameworks is essential to bridge the gap between laboratory research and practical deployment of these advanced MEPCMs in energy storage, smart coatings, and building materials.

Author Contributions: Conceptualization, B.D. and C.Y.; methodology, B.D. and C.Y.; investigation, C.Y.; formal analysis, B.D. and C.Y.; writing—original draft, C.Y.; writing—review and editing, B.D. and C.Y.; supervision, B.D.; funding acquisition, B.D. All authors have read and agreed to the published version of the manuscript.

Funding: This research was funded by the National Natural Science Foundation of China, grant number 52473020.

Data Availability Statement: No new data were created or analyzed in this study. Data sharing is not applicable to this article.

Conflicts of Interest: The authors declare no conflicts of interest.

Abbreviations

The following abbreviations are used in this manuscript:

ACQ	Aggregation-caused quenching
BS	Butyl stearate
CA	Capric acid
CB	Carbon black
CDQs	Carbon quantum dots
CNC	Cellulose nanocrystal
CNT	Carbon nanotube
CS	Chitosan
CTAB	Cetyl trimethyl ammonium bromide
DPP	Diketopyrrolopyrrole
DSC	Differential scanning calorimetry
EC	Ethyl cellulose
GO	Graphene oxide
HF	Hydrofluoric acid
HLB	Hydrophilic and lipophilic balance
ICG	Indocyanine green
LA	Lauric acid
LHS	Latent heat storage
LSPR	Localized surface plasmon resonance
LTH	Light-to-hydrogen
MB	Methylene blue
MEPCMs	Microencapsulated phase-change materials
MF	Melamine-formaldehyde
MIP	Molecularly imprinted polymer
NG	Nano-graphite
PA	Paraffin
PANI	Polyaniline
PB	Prussian blue

PCMs	Phase-change materials
PDA	Polydopamine
PMMA	Polymethyl methacrylate
PPY	Polypyrrole
PS	Polystyrene
PU	Polyurethane
PUA	Polyurethane acrylates
PVP	Polyvinylpyrrolidone
RhB	Rhodamine B
rGO	Reduced graphene oxide
SDB	Styrene divinylbenzene
SDBS	Sodium dodecyl-benzenesulfonate
SHS	Sensible heat storage
TCHS	Thermal chemical heat storage
TEOS	Tetraethoxysilane
TES	Thermal energy storage
UF	Urea-formaldehyde
Vis-NIR	Visible-to-near-infrared

References

1. Borge-Diez, D. Energy Policy, Energy Research, and Energy Politics: An Analytical Review of the Current Situation. *Energies* **2022**, *15*, 8792. [CrossRef]
2. Rode, A.; Carleton, T.; Delgado, M.; Greenstone, M.; Houser, T.; Hsiang, S.; Hultgren, A.; Jina, A.; Kopp, R.E.; McCusker, K.E.; et al. Estimating a social cost of carbon for global energy consumption. *Nature* **2021**, *598*, 308–314. [CrossRef] [PubMed]
3. Jafarizadeh, H.; Soltani, M.; Alfraidi, W. A comprehensive Thermoeconomic assessment of liquid air and compressed air energy storage with solid/liquid/hybrid thermal energy storage (TES): Addressing air and TES material storage cost impacts. *Appl. Energy* **2025**, *388*, 125615. [CrossRef]
4. Sifnaios, I.; Sneum, D.M.; Jensen, A.R.; Fan, J.; Bramstoft, R. The impact of large-scale thermal energy storage in the energy system. *Appl. Energy* **2023**, *349*, 121663. [CrossRef]
5. Zhang, P.; Ma, F.; Xiao, X. Thermal energy storage and retrieval characteristics of a molten-salt latent heat thermal energy storage system. *Appl. Energy* **2016**, *173*, 255–271. [CrossRef]
6. Ghaib, K. Latent Heat Storage: Storage Materials, Heat Transfer, and Applications. *Chem. Ing. Tech.* **2017**, *89*, 1115–1125. [CrossRef]
7. Zhang, C.; Huang, Y.; Chen, Y. Bionic study on latent heat thermal storage. *Renew. Sustain. Energy Rev.* **2023**, *183*, 113529. [CrossRef]
8. Rezaei, E.; Barbato, M.; Ortona, A.; Haussener, S. Design and optimization of a high-temperature latent heat storage unit. *Appl. Energy* **2020**, *261*, 114330. [CrossRef]
9. Lu, J.; Zhang, T.; Xu, Z.; Zhao, Y. Octodecane-cellulose nanofiber flexible composites for latent heat storage. *Chem. Eng. J.* **2021**, *425*, 131432. [CrossRef]
10. Jafarian, M.; Arjomandi, M.; Nathan, G.J. A hybrid solar and chemical looping combustion system for solar thermal energy storage. *Appl. Energy* **2013**, *103*, 671–678. [CrossRef]
11. Zhao, J.; Korba, D.; Mishra, A.; Klausner, J.; Randhir, K.; AuYeung, N.; Li, L. Particle-based high-temperature thermochemical energy storage reactors. *Prog. Energy Combust. Sci.* **2024**, *102*, 101143. [CrossRef]
12. Zhou, Y.; Zhou, Z.; Sun, J.; Liu, L.; Luo, F.; Xu, G.; Cao, X.E.; Xu, M. Ruddlesden-Popper-type perovskite $Sr_3Fe_2O_7-\delta$ for enhanced thermochemical energy storage. *EcoMat* **2023**, *5*, e12347. [CrossRef]
13. Sommer, W.; Valstar, J.; Leusbrock, I.; Grotenhuis, T.; Rijnaarts, H. Optimization and spatial pattern of large-scale aquifer thermal energy storage. *Appl. Energy* **2015**, *137*, 322–337. [CrossRef]
14. Zhao, Y.; Song, J.; Liu, M.; Zhao, Y.; Olympios, A.V.; Sapin, P.; Yan, J.; Markides, C.N. Thermo-economic assessments of pumped-thermal electricity storage systems employing sensible heat storage materials. *Renew. Energy* **2022**, *186*, 431–456. [CrossRef]
15. Seyitini, L.; Belgasim, B.; Enweremadu, C.C. Solid state sensible heat storage technology for industrial applications—A review. *J. Energy Storage* **2023**, *62*, 106919. [CrossRef]
16. Mishra, R.K.; Verma, K.; Mishra, V.; Chaudhary, B. A review on carbon-based phase change materials for thermal energy storage. *J. Energy Storage* **2022**, *50*, 104166. [CrossRef]

17. Nazir, H.; Batool, M.; Osorio, F.J.B.; Isaza-Ruiz, M.; Xu, X.H.; Vignarooban, K.; Phelan, P.; Inamuddin; Kannan, A.M. Recent developments in phase change materials for energy storage applications: A review. *Int. J. Heat Mass Transfer* **2019**, *129*, 491–523. [CrossRef]
18. Sun, M.Y.; Liu, T.; Sha, H.A.; Li, M.L.; Liu, T.Z.; Wang, X.L.; Chen, G.J.; Wang, J.D.; Jiang, D.Y. A review on thermal energy storage with eutectic phase change materials: Fundamentals and applications. *J. Energy Storage* **2023**, *68*, 107713. [CrossRef]
19. Usman, A.; Xiong, F.; Aftab, W.; Qin, M.L.; Zou, R.Q. Emerging Solid-to-Solid Phase-Change Materials for Thermal-Energy Harvesting, Storage, and Utilization. *Adv. Mater.* **2022**, *34*, 2202457. [CrossRef]
20. Rostami, S.; Afrand, M.; Shahsavar, A.; Sheikholeslami, M.; Kalbasi, R.; Aghakhani, S.; Shadloo, M.S.; Oztop, H.F. A review of melting and freezing processes of PCM/nano-PCM and their application in energy storage. *Energy* **2020**, *211*, 118698. [CrossRef]
21. Li, X.; Liu, Y.; Xu, Y.; Tao, P.; Deng, T. Solid–Liquid Phase Change Composite Materials for Direct Solar–Thermal Energy Harvesting and Storage. *Acc. Mater. Res.* **2023**, *4*, 484–495. [CrossRef]
22. Su, W.G.; Darkwa, J.; Kokogiannakis, G. Review of solid-liquid phase change materials and their encapsulation technologies. *Renew. Sustain. Energy Rev.* **2015**, *48*, 373–391. [CrossRef]
23. Liu, L.; Alva, G.; Huang, X.; Fang, G. Preparation, heat transfer and flow properties of microencapsulated phase change materials for thermal energy storage. *Renew. Sustain. Energy Rev.* **2016**, *66*, 399–414. [CrossRef]
24. Németh, B.; Németh, Á.S.; Ujhidy, A.; Tóth, J.; Trif, L.; Jankovics, H.; Kriszt, B.; Dobolyi, C.; May, Z.; Gyenis, J.; et al. Antimicrobial functionalization of Ca alginate-coconut oil latent heat storing microcapsules by Ag nanoparticles. *Int. J. Energy Res.* **2020**, *44*, 11998–12014. [CrossRef]
25. Li, Y.; Jiang, Z.; He, F.; Chen, Z.; Li, X.; Wang, P.; He, G.; Zhu, X.; Yang, W. Reversible thermochromic microcapsules with SiO_2 shell for indicating temperature and thermoregulation. *J. Energy Storage* **2023**, *72*, 108674. [CrossRef]
26. Ke, W.-D.; Wu, X.-W.; Zhang, J.-L. In situ polymerization of organic and inorganic phase change microcapsule and enhancement of infrared stealth via nano iron. *Colloids Surf. A* **2021**, *627*, 127124. [CrossRef]
27. Shen, H.; Zheng, Z.; Liu, H.; Wang, X. A solar-powered interfacial evaporation system based on MoS_2-decorated magnetic phase-change microcapsules for sustainable seawater desalination. *J. Mater. Chem. A* **2022**, *10*, 25509–25526. [CrossRef]
28. Tang, Z.D.; Gao, H.Y.; Chen, X.; Zhang, Y.F.; Li, A.; Wang, G. Advanced multifunctional composite phase change materials based on photo-responsive materials. *Nano Energy* **2021**, *80*, 105454. [CrossRef]
29. Jiang, Z.; Yang, W.; He, F.; Xie, C.; Fan, J.; Wu, J.; Zhang, K. Modified Phase Change Microcapsules with Calcium Carbonate and Graphene Oxide Shells for Enhanced Energy Storage and Leakage Prevention. *ACS Sustain. Chem. Eng.* **2018**, *6*, 5182–5191. [CrossRef]
30. Li, X.; Hu, M.; Liu, M.; Wang, Z.; Yu, J.; Guo, J. Preparation of hydrated calcium silicate phase change microcapsules and its application of temperature regulation in deep-water natural gas hydrate layer cementing process. *Constr. Build. Mater.* **2024**, *428*, 136413. [CrossRef]
31. Li, Y.; Xu, L.; Jiang, Z.; Li, Y.; He, F.; Zhang, K.; He, R.; Chen, Z.; Yang, W. Paraffin@poly(methyl methacrylate) Phase Change Microcapsules for Thermal Energy Storage and Temperature Regulation. *ChemistrySelect* **2023**, *8*, e202203857. [CrossRef]
32. Yan, B.; Lu, H.; Li, M.; Wang, X.; Wang, Z.; Pi, M.; Cui, W.; Ran, R. Preparation of phase change microcapsules with high thermal storage and temperature sensitive for thermal management. *J. Energy Storage* **2023**, *64*, 107003. [CrossRef]
33. Su, J.; Zhang, H.; Gong, Y.; Xu, Q.; Hou, M.; Xu, B. Fabrication and properties analysis of paraffin@TiO_2/Ag phase change microcapsules for thermal energy storage and photocatalysis. *Mater. Sci. Eng. B* **2024**, *301*, 117150. [CrossRef]
34. Chang, Z.J.; Wang, K.; Wu, X.H.; Lei, G.; Wang, Q.W.; Liu, H.; Wang, Y.L.; Zhang, Q. Review on the preparation and performance of paraffin-based phase change microcapsules for heat storage. *J. Energy Storage* **2022**, *46*, 103840. [CrossRef]
35. Li, S.-Y.; Yan, T.; Wang, K.-W.; Xie, T.; Pan, W.-G. Paraffin wax@TiO_2 phase change microcapsules in SiC-doped for solar energy conversion and thermal storage. *Sol. Energy Mater. Sol. Cells* **2025**, *282*, 113395. [CrossRef]
36. Chen, C.; Fang, L.; Wang, Y.; Jiu, S.; Chen, Y. Mechanical, thermal and microscopic properties of gypsum matrix composites containing capric acid-palmitic acid/urea-formaldehyde microcapsules. *Case Stud. Constr. Mater.* **2023**, *18*, e02084. [CrossRef]
37. Ma, J.; Liu, H.; Sun, D.; Wang, J.; Cui, S. Synthesis of phase change microcapsules with binary fatty acid ester core and their feasibility investigation in energy conservation of cementitious materials. *Constr. Build. Mater.* **2022**, *330*, 127212. [CrossRef]
38. Feng, Y.; Sun, S.-L.; Yu, S.-B.; Lin, C.-H.; Ning, Y.-H.; Li, Q.; Zhang, Y.-H.; Zhou, M.; Li, Y.-T.; Wang, S.-F.; et al. Effects of in-situ acid dopants on the latent heat storage properties and morphology of palmitic acid @ polyaniline microencapsulated phase change materials. *Colloids Surf. A* **2022**, *647*, 129207. [CrossRef]
39. Gulfam, R.; Zhang, P.; Meng, Z. Advanced thermal systems driven by paraffin-based phase change materials – A review. *Appl. Energy* **2019**, *238*, 582–611. [CrossRef]
40. Zhang, Z.; Lian, Y.; Xu, X.; Xu, X.; Fang, G.; Gu, M. Synthesis and characterization of microencapsulated sodium sulfate decahydrate as phase change energy storage materials. *Appl. Energy* **2019**, *255*, 113830. [CrossRef]
41. Wang, K.; Zhang, T.; Wang, T.; Xu, C.; Ye, F.; Liao, Z. Microencapsulation of high temperature metallic phase change materials with SiCN shell. *Chem. Eng. J.* **2022**, *436*, 135054. [CrossRef]

42. Wang, S.; Lei, K.; Wang, Z.; Wang, H.; Zou, D. Metal-based phase change material (PCM) microcapsules/nanocapsules: Fabrication, thermophysical characterization and application. *Chem. Eng. J.* **2022**, *438*, 135559. [CrossRef]
43. Kawaguchi, T.; Nakamura, T.; Kondo, M.; Chidiebere Mba, J.; Dong, K.; Shimizu, Y.; Jeem, M.; Nomura, T. Microencapsulation of Zn-10 mass% Al alloy phase change material via dry synthesis method. *Chem. Eng. J.* **2024**, *498*, 154782. [CrossRef]
44. Wang, K.; Tao, K.; Guo, M.; Wang, T.; Liao, Z.; Ye, F.; Xu, C.; Du, X. Thermal and cyclic performance of aluminum alloy composite phase change microcapsules for high-temperature thermal energy storage. *Sol. Energy Mater. Sol. Cells* **2024**, *277*, 113128. [CrossRef]
45. Gu, M.; Huang, Y.; Bao, K.; Wang, L.; Huang, T.; Li, Y.; Cheng, X. Efficient preparation of GO-modified regular spherical SiO_2@$CaCl_2 \cdot 6H_2O$ phase change microcapsules for enhanced thermal energy storage. *J. Energy Storage* **2024**, *83*, 110727. [CrossRef]
46. Zhang, X.; Yang, Y.; Zhong, C.; Xiang, D.; Sun, H.; Li, D.; Yan, G.; Wu, Y. High-Performance Phase Change Films Prepared by a Strategy for Thermal Management at Interfaces and Environmental Camouflage. *Small* **2025**, *21*, 2500683. [CrossRef]
47. Raj, C.R.; Suresh, S.; Bhavsar, R.R.; Kumar Singh, V.; Reddy, S. Effect of nano-gallium capsules on thermal energy storage characteristics of manganese organometallic SS-PCM. *Thermochim. Acta* **2019**, *680*, 178341. [CrossRef]
48. Bao, J.; Zou, D.; Zhu, S.; Ma, Q.; Wang, Y.; Hu, Y. A medium-temperature, metal-based, microencapsulated phase change material with a void for thermal expansion. *Chem. Eng. J.* **2021**, *415*, 128965. [CrossRef]
49. Sheng, N.; Lu, J.; Hu, J.; Zhu, R.; Fadillah, L.; Wang, C.; Zhu, C.; Rao, Z.; Habazaki, H. Synthesis of Sn@SnO_2 core-shell microcapsules by a self-oxidation strategy for medium temperature thermal storage. *Chem. Eng. J.* **2021**, *420*, 129906. [CrossRef]
50. Zhu, C.; Liu, R.; Lu, J.; Sheng, N. Preparation of Microencapsulated Low-Melting-Point Sn–Bi Alloy for Latent Heat Storage. *Energy Technol.* **2022**, *11*, 2201068. [CrossRef]
51. Gokon, N.; Jie, C.S.; Nakano, Y.; Okazaki, S.; Kodama, T.; Hatamachi, T.; Bellan, S. Phase Change Material of Copper–Germanium Alloy as Solar Latent Heat Storage at High Temperatures. *Front. Energy Res.* **2021**, *9*, 696213. [CrossRef]
52. Nomura, T.; Yoolerd, J.; Sheng, N.; Sakai, H.; Hasegawa, Y.; Haga, M.; Akiyama, T. Al/Al_2O_3 core/shell microencapsulated phase change material for high-temperature applications. *Sol. Energy Mater. Sol. Cells* **2019**, *193*, 281–286. [CrossRef]
53. Han, C.; Gu, H.; Zhang, M.; Huang, A.; Zhang, Y.; Wang, Y. Al–Si @ Al_2O_3 @ mullite microcapsules for thermal energy storage: Preparation and thermal properties. *Sol. Energy Mater. Sol. Cells* **2020**, *217*, 110697. [CrossRef]
54. Zhang, Z.; Zhang, Z.; Chang, T.; Wang, J.; Wang, X.; Zhou, G. Phase change material microcapsules with melamine resin shell via cellulose nanocrystal stabilized Pickering emulsion in-situ polymerization. *Chem. Eng. J.* **2022**, *428*, 131164. [CrossRef]
55. Trivedi, G.V.N.; Parameshwaran, R. Cryogenic conditioning of microencapsulated phase change material for thermal energy storage. *Sci. Rep.* **2020**, *10*, 18353. [CrossRef]
56. Li, F.; Sun, Z.; Jiao, S.; Ma, Y.; Zhang, Q.; Zhou, Y.; Wen, J.; Liu, Y. Preparation and Performance of Dual-functional Magnetic Phase-change Microcapsules. *Chem. Asian J.* **2020**, *16*, 102–109. [CrossRef]
57. Chang, Y.; Sun, Z. Synthesis and thermal properties of *n*-tetradecane phase change microcapsules for cold storage. *J. Energy Storage* **2022**, *52*, 104959. [CrossRef]
58. Wang, X.; Chen, Z.; Xu, W.; Wang, X. Capric acid phase change microcapsules modified with graphene oxide for energy storage. *J. Mater. Sci.* **2019**, *54*, 14834–14844. [CrossRef]
59. Yan, J.; Ruan, L.; Hu, D.; Liu, W.; Chen, W.; Ma, W. Microencapsulation of Phase Change Materials with a Soy Oil-Based Polyurethane Shell via Pickering Emulsion Polymerization. *ACS Appl. Energy Mater.* **2023**, *6*, 6814–6825. [CrossRef]
60. Li, C.; Fu, J.; Huang, F.; Zhu, Z.; Si, T. Controlled Latent Heat Phase-Change Microcapsules for Temperature Regulation. *ACS Appl. Mater. Interfaces* **2023**, *15*, 30383–30393. [CrossRef]
61. Chen, L.; Lao, J.; Ma, J.; He, Z.; Fu, W.; Liu, J.; Peng, H.; Fang, T.; Luo, Y. Synthesis and properties of methyl palmitate-polyurea phase change microcapsules. *Polymer* **2025**, *319*, 128073. [CrossRef]
62. Huang, H.; Shi, T.; He, R.; Wang, J.; Chu, P.K.; Yu, X.F. Phase-Changing Microcapsules Incorporated with Black Phosphorus for Efficient Solar Energy Storage. *Adv. Sci.* **2020**, *7*, 2000602. [CrossRef]
63. Zhang, W.; Pan, R.; Yang, J.; Liu, M.; Yao, Y.; Zhang, A.; Gong, Y.; Gan, Z.; Hu, R.; Ding, J.; et al. Polystyrene shell-based "coconut-like" and "pomegranate-like" microencapsulated phase change materials: Formation mechanism, thermal conductivity/stability enhancement and their application in thermal management. *Chem. Eng. J.* **2024**, *498*, 155758. [CrossRef]
64. Xu, C.; Gou, W.; Wang, X.; Zhou, J.; Liu, J.; Chen, K. Synthesis of paraffin@PS/reduced graphene oxide microcapsules via Pickering emulsion for multi-protective coatings. *Colloids Surf. A* **2021**, *613*, 126054. [CrossRef]
65. Zhang, W.; Cheng, H.; Pan, R.; Yang, J.H.; Gong, Y.; Gan, Z.; Hu, R.; Ding, J.; Chen, L.; Zhang, X.; et al. Phase Change Microcapsules with a Polystyrene/Boron Nitride Nanosheet Hybrid Shell for Enhanced Thermal Management of Electronics. *Langmuir* **2022**, *38*, 16055–16066. [CrossRef] [PubMed]
66. Chen, M.; Qian, Z.; Liu, H.; Wang, X. Size-tunable $CaCO_3$@*n*-eicosane phase-change microcapsules for thermal energy storage. *Colloids Surf. A* **2022**, *640*, 128470. [CrossRef]
67. Liu, H.; Tian, D.; Ouyang, M.; Qian, Z.; Wang, X. Morphology-controlled fabrication of magnetic phase-change microcapsules for synchronous efficient recovery of wastewater and waste heat. *J. Colloid Interface Sci.* **2022**, *608*, 1497–1513. [CrossRef]

68. Zhang, M.; Shen, H.; Qian, Z.; Liu, H.; Tian, D.; Wang, X. Dual-purpose applications of magnetic phase-change microcapsules with crystalline-phase-tunable $CaCO_3$ shell for waste heat recovery and heavy metal ion removal. *J. Energy Storage* **2022**, *55*, 105672. [CrossRef]
69. Wang, B.; Shi, M.; Yao, H.; Yang, X.; Guo, S.; Liu, Y.; Hua, Q.; Shen, B.; Liu, P.; Tang, J. Preparation and application of low-temperature binary eutectic lauric acid-stearic acidSiO_2 phase change microcapsules. *Energy Build.* **2023**, *279*, 112706. [CrossRef]
70. Sun, Z.; Sun, K.; Zhang, H.; Liu, H.; Wu, D.; Wang, X. Development of poly(ethylene glycol)/silica phase-change microcapsules with well-defined core-shell structure for reliable and durable heat energy storage. *Sol. Energy Mater. Sol. Cells* **2021**, *225*, 111069. [CrossRef]
71. Sun, Z.; Han, Z.; Liu, H.; Wu, D.; Wang, X. Nanoflaky nickel-hydroxide-decorated phase-change microcapsules as smart electrode materials with thermal self-regulation function for supercapacitor application. *Renew. Energy* **2021**, *174*, 557–572. [CrossRef]
72. Zhu, H.; Li, M.; Yi, H.; Jia, F.; Xu, J.; Song, S. Paraffin@Hectorite-SiO_2/Fe_3O_4 microcapsule phase change fluid for efficient photothermal energy storage and heat dissipation. *Appl. Clay Sci.* **2025**, *271*, 107797. [CrossRef]
73. Cheng, H.; Tang, B.; Bao, H.Y.; Shan, F.; Lu, C.X. Preparation and application of high thermal conductivity phase change microcapsules with fluorescence characteristics based on a $ZnWO_4$ shell. *Nanoscale* **2024**, *16*, 20331–20341. [CrossRef] [PubMed]
74. Hu, T.; Zhang, J.; Xiao, R.; Wang, G.; Yu, W.; Su, H.; Su, L. Study on the preparation and properties of TiO_2@*n*-octadecane phase change microcapsules for regulating building temperature. *Appl. Therm. Eng.* **2024**, *249*, 123429. [CrossRef]
75. Li, M.; Liu, J.; Shi, J. Synthesis and properties of phase change microcapsule with SiO_2-TiO_2 hybrid shell. *Sol. Energy* **2018**, *167*, 158–164. [CrossRef]
76. Chen, S.; Liu, H.; Wang, X. Pomegranate-like phase-change microcapsules based on multichambered TiO_2 shell engulfing multiple *n*-docosane cores for enhancing heat transfer and leakage prevention. *J. Energy Storage* **2022**, *51*, 104406. [CrossRef]
77. Wang, X.; Wu, Y.; Zou, F.; Jin, L.; Zhong, Y.; Ma, C. Thermal and photocatalytic properties of TiO_2 hybrid phase change microcapsules. *J. Energy Storage* **2024**, *102*, 114164. [CrossRef]
78. Wang, X.; Chen, H.; Kuang, D.; Huan, X.; Zeng, Z.; Qi, C.; Han, S.; Li, G. Unlocking thermal management capacity: Optimized organic-inorganic hybrid shell phase change microcapsules with controllable structure and enhanced conductivity. *Compos. Sci. Technol.* **2024**, *257*, 110836. [CrossRef]
79. Hu, T.; Zhang, J.; Chan, W.; Xiao, R.; Xu, H.; Zhao, X.; Wang, G.; Yu, W. Synthesis and optimization of GO/TiO_2@*n*-octadecane microcapsules for thermal management of smartphone charging. *Appl. Therm. Eng.* **2024**, *257*, 124409. [CrossRef]
80. Paswan, R.; Das, S. Elucidating the evolution of pore structure, microstructural damage, and micromechanical response in cement pastes containing microencapsulated phase change materials under freeze-thaw conditions. *Cem. Concr. Compos.* **2024**, *154*, 105743. [CrossRef]
81. Yao, C.; Yu, X.; Feng, L.; Wang, F.; Wang, M.; Yuan, Q. Development of microencapsulated phase change material slurry for diamond wire sawing silicon wafer and its effect on cutting quality. *J. Manuf. Process.* **2024**, *127*, 421–432. [CrossRef]
82. Sun, W.; Zhang, Z.; Zhang, Z.; He, N.; Wei, Q.; Feng, L.; Wang, Z.; Wu, J.; Liu, C.; Fu, S.; et al. Photothermal phase change material microcapsules via cellulose nanocrystal and graphene oxide co-stabilized Pickering emulsion for solar and thermal energy storage. *Sci. China Mater.* **2024**, *67*, 3225–3235. [CrossRef]
83. Gu, B.; Li, G.; Zhang, Q.; Pan, H.; Duan, M.; Weng, L.; Zhao, D. A Novel Method for Increasing Phase-Change Microcapsules in Nanofiber Textile through Electrospinning. *Adv. Funct. Mater.* **2024**, *35*, 2412089. [CrossRef]
84. Sun, L.; Wang, Y.; Chen, L.; Ying, J.; Li, Q.; Fu, L.; Yan, Q.; Wu, K.; Xue, C.; Yu, J.; et al. van der Waals-bonded graphene clusters enhance thermal conductivity of phase-change materials for advanced thermal energy management. *Mater. Horiz.* **2024**, *11*, 5031–5044. [CrossRef] [PubMed]
85. Jing, J.; Liu, H.; Wang, X. Multifunctional BiOI/SiO_2/Fe_3O_4@*n*-Docosane Phase-Change Microcapsules for Waste Heat Recovery and Wastewater Treatment. *Materials* **2023**, *16*, 1656. [CrossRef]
86. Wang, M.; Liu, G.; Gao, H.; Su, C.; Gao, J. Preparation and performance of reversible thermochromic phase change microcapsules based on negative photochromic spiropyran. *Colloids Surf. A* **2023**, *659*, 130808. [CrossRef]
87. Cheng, P.F.; Wang, D.; Schaaf, P. A Review on Photothermal Conversion of Solar Energy with Nanomaterials and Nanostructures: From Fundamentals to Applications. *Adv. Sustain. Syst.* **2022**, *6*, 2200115. [CrossRef]
88. Liu, H.; Wang, X.; Wu, D. Fabrication of Graphene/TiO_2/Paraffin Composite Phase Change Materials for Enhancement of Solar Energy Efficiency in Photocatalysis and Latent Heat Storage. *ACS Sustain. Chem. Eng.* **2017**, *5*, 4906–4915. [CrossRef]
89. Yu, Y.; He, L.; Lu, P.; Yuan, Y.; Zhang, H. Preparation, performances and applications of multi-functional photoluminescence form-stable phase change materials. *Polymer* **2020**, *189*, 122211. [CrossRef]
90. Cui, X.M.; Ruan, Q.F.; Zhu, X.L.; Xia, X.Y.; Hu, J.T.; Fu, R.F.; Li, Y.; Wang, J.F.; Xu, H.X. Photothermal Nanomaterials: A Powerful Light-to-Heat Converter. *Chem. Rev.* **2023**, *123*, 6891–6952. [CrossRef]
91. Li, Z.J.; Lei, H.; Kan, A.K.; Xie, H.Q.; Yu, W. Photothermal applications based on graphene and its derivatives: A state-of-the-art review. *Energy* **2021**, *216*, 119262. [CrossRef]

92. Ren, J.; Hu, T.; Zhang, W.; Li, L.; Yuan, W. Enhanced photo-thermal conversion in phase change materials by Cu-Zn Bi-metallic metal-organic framework and expanded graphite. *Sol. Energy Mater. Sol. Cells* **2025**, *281*, 113326. [CrossRef]
93. Li, A.; Huang, M.; Hu, D.; Tang, Z.; Xu, J.; Li, Y.; Zhang, X.; Chen, X.; Wang, G. Polydopamine-coated metal-organic framework-based composite phase change materials for photothermal conversion and storage. *Chin. Chem. Lett.* **2023**, *34*, 107916. [CrossRef]
94. Li, J.; Chen, Y.; Xu, J.; Zhang, F. Preparation and energy storage application of polydopamine-modified silica phase change microcapsules. *Mater. Today Commun.* **2025**, *46*, 112694. [CrossRef]
95. Zeng, W.A.; Ye, X.Y.; Dong, Y.C.; Zhang, Y.Q.; Sun, C.Z.; Zhang, T.; Guan, X.J.; Guo, L.J. MXene for photocatalysis and photothermal conversion: Synthesis, physicochemical properties, and applications. *Coord. Chem. Rev.* **2024**, *508*, 215753. [CrossRef]
96. Shi, L.; Huang, C.; Zheng, N.; Chen, J.; Ning, R.; Huang, Z.; Deng, N.; Fang, X.; Zhou, T.; Sun, Z. Thermal energy storage characteristics of carbon-based phase change composites for photo-thermal conversion. *J. Energy Storage* **2024**, *77*, 109892. [CrossRef]
97. Shen, Y.; Skirtach, A.G.; Seki, T.; Yagai, S.; Li, H.; Möhwald, H.; Nakanishi, T. Assembly of Fullerene-Carbon Nanotubes: Temperature Indicator for Photothermal Conversion. *J. Am. Chem. Soc.* **2010**, *132*, 8566–8568. [CrossRef]
98. Lim, D.-K.; Barhoumi, A.; Wylie, R.G.; Reznor, G.; Langer, R.S.; Kohane, D.S. Enhanced Photothermal Effect of Plasmonic Nanoparticles Coated with Reduced Graphene Oxide. *Nano Lett.* **2013**, *13*, 4075–4079. [CrossRef]
99. Prasher, R. Graphene Spreads the Heat. *Science* **2010**, *328*, 185–186. [CrossRef]
100. Li, J.; Jia, L.; Li, L.; Huang, Z.; Chen, Y. Hybrid Microencapsulated Phase-Change Material and Carbon Nanotube Suspensions toward Solar Energy Conversion and Storage. *Energies* **2020**, *13*, 4401. [CrossRef]
101. Chen, S.; Zheng, Z.; Liu, H.; Wang, X. Highly Efficient, Antibacterial, and Salt-Resistant Strategy Based on Carbon Black/Chitosan-Decorated Phase-Change Microcapsules for Solar-Powered Seawater Desalination. *ACS Appl. Mater. Interfaces* **2023**, *15*, 16640–16653. [CrossRef]
102. Yuan, K.; Chen, Q.; Zhang, A.; Xiao, N.; Zou, X.; Lin, Z. Efficient thermal energy conversion and storage enabled by hybrid graphite nanoparticles/silica-encapsulated phase-change microcapsules. *J. Mater. Chem. A* **2024**, *12*, 2456–2464. [CrossRef]
103. Guo, S.; Gu, D.Y.; Yang, Y.; Tian, J.; Chen, X.Y. Near-infrared photodynamic and photothermal co-therapy based on organic small molecular dyes. *J. Nanobiotechnol.* **2023**, *21*, 348. [CrossRef]
104. Kim, H.J.; Kim, B.; Auh, Y.; Kim, E. Conjugated Organic Photothermal Films for Spatiotemporal Thermal Engineering. *Adv. Mater.* **2021**, *33*, 2005940. [CrossRef]
105. Yuan, S.; Yan, R.; Ren, B.; Du, Z.; Cheng, X.; Du, X.; Wang, H. Robust, double-layered phase-changing microcapsules with superior solar-thermal conversion capability and extremely high energy storage density for efficient solar energy storage. *Renew. Energy* **2021**, *180*, 725–733. [CrossRef]
106. Zhang, Q.; Chen, Y.; Liu, R.; Luo, J. Efficiently all-weather anti-icing and de-icing coatings enabled by polyaniline microcapsules encapsulated phase change materials. *Chem. Eng. J.* **2024**, *499*, 156122. [CrossRef]
107. Li, M.; Chang, P.; Pan, Y. Preparation and performance improvement of poly-pyrrole modified yeast phase change microcapsules for photothermal energy conversion and storage. *Sol. Energy* **2025**, *286*, 113180. [CrossRef]
108. Li, P.; Zou, F.; Wang, X.; Kamal Alebeid, O.; Zhao, T. In-situ deposition preparation of *n*-octadecane@Silica@Polydopamine-doped polypyrrole microcapsules for photothermal conversion and thermal energy storage of full-spectrum solar radiation. *Sol. Energy* **2022**, *240*, 388–398. [CrossRef]
109. Li, X.; Jiang, H.; Ma, C.; Zhu, Z.; Song, X.; Wang, H.; Huo, P.; Li, X. Local surface plasma resonance effect enhanced Z-scheme ZnO/Au/g-C_3N_4 film photocatalyst for reduction of CO_2 to CO. *Appl. Catal. B* **2021**, *283*, 119638. [CrossRef]
110. Li, J.; Zhang, N.; Li, D.; Li, Y.; Zhang, W.; Zhao, Z.; Song, S.; Liu, Y.; Qin, L.; Bao, X.; et al. Construction of medium-entropy alloys coupled Z-Scheme heterojunction and its enhanced photocatalytic performance by regulating mechanism of LSPR effect. *J. Mater. Sci. Technol.* **2024**, *197*, 32–45. [CrossRef]
111. Zhou, F.; Ma, Y.; Zhao, W.; Zhang, L.; Chen, Y.; Sheng, X. Integrating AgNPs-decorated phase change microcapsules into UV-cured PUA with enhanced thermal conductivity for solar thermal energy conversion and storage. *Sol. Energy Mater. Sol. Cells* **2025**, *279*, 113253. [CrossRef]
112. Peng, S.; Zhong, W.; Zhao, H.; Wang, C.; Tian, Z.; Shu, R.; Chen, Y. Solar-driven multifunctional Au/TiO_2@PCM towards bio-glycerol photothermal reforming hydrogen production and thermal storage. *Int. J. Hydrogen Energy* **2022**, *47*, 41573–41586. [CrossRef]
113. Luo, W.; Zou, M.; Wang, J.; Ma, Y.; Hu, X.; Chen, W.; Jiang, X. Polypyrrole and Ag nanoparticles synergistically enhances the photothermal conversion performance of microencapsulated phase change energy storage materials in multiple way. *Sol. Energy Mater. Sol. Cells* **2025**, *283*, 113451. [CrossRef]
114. Zhang, D.; Yang, A.-S.; Jiang, Z.; He, F.; Li, Y.; Li, X.; Chen, Z.; Yang, W. Paraffin@silica@poly(dopamine)/Silver Phase Change Microcapsules with Efficient Photothermal Conversion Performance. *Energy Fuels* **2023**, *37*, 16951–16961. [CrossRef]

115. Naguib, M.; Kurtoglu, M.; Presser, V.; Lu, J.; Niu, J.; Heon, M.; Hultman, L.; Gogotsi, Y.; Barsoum, M.W. Two-Dimensional Nanocrystals Produced by Exfoliation of Ti_3AlC_2. *Adv. Mater.* **2011**, *23*, 4248–4253. [CrossRef]
116. Alhabeb, M.; Maleski, K.; Mathis, T.S.; Sarycheva, A.; Hatter, C.B.; Uzun, S.; Levitt, A.; Gogotsi, Y. Selective Etching of Silicon from Ti_3SiC_2 (MAX) To Obtain 2D Titanium Carbide (MXene). *Angew. Chem. Int. Ed.* **2018**, *57*, 5444–5448. [CrossRef]
117. Hantanasirisakul, K.; Gogotsi, Y. Electronic and Optical Properties of 2D Transition Metal Carbides and Nitrides (MXenes). *Adv. Mater.* **2018**, *30*, 1804779. [CrossRef]
118. Naguib, M.; Barsoum, M.W.; Gogotsi, Y. Ten Years of Progress in the Synthesis and Development of MXenes. *Adv. Mater.* **2021**, *33*, 2103393. [CrossRef]
119. Zhao, K.; Guo, Z.; Wang, J.; Xie, H. Enhancing solar photothermal conversion and energy storage with titanium carbide (Ti_3C_2) MXene nanosheets in phase-change microcapsules. *J. Colloid Interface Sci.* **2023**, *650*, 1591–1604. [CrossRef]
120. Zhang, M.; Sun, K.; Zheng, Z.; Liu, H.; Wang, X. Development of MXene-decorated sodium alginate/SiO_2@*n*-docosane hierarchical phase-change microcapsules for solar-driven sustainable seawater desalination. *Desalination* **2023**, *550*, 116380. [CrossRef]
121. Lu, J.; Deng, Y.; Luo, D.; Wu, F.; Dai, X. Preparation and performance enhancement of MXene/$Na_2HPO_4{\cdot}12H_2O$@SiO_2 phase change microcapsule. *J. Energy Storage* **2024**, *91*, 112079. [CrossRef]
122. Gancheva, M.; Markova-Velichkova, M.; Atanasova, G.; Kovacheva, D.; Uzunov, I.; Cukeva, R. Design and photocatalytic activity of nanosized zinc oxides. *Appl. Surf. Sci.* **2016**, *368*, 258–266. [CrossRef]
123. Arsha Kusumam, T.V.; Panakkal, T.; Divya, T.; Nikhila, M.P.; Anju, M.; Anas, K.; Renuka, N.K. Morphology controlled synthesis and photocatalytic activity of zinc oxide nanostructures. *Ceram. Int.* **2016**, *42*, 3769–3775. [CrossRef]
124. Chen, H.; Liu, X.; Zhao, K.; Wang, J.; Xie, H. Preparation of PW@$CaCO_3$ phase change microcapsules modified by ZnO nanoparticles with excellent photocatalytic and thermal properties. *J. Energy Storage* **2024**, *77*, 109942. [CrossRef]
125. Kumar, R.; Abdel-Wahab, M.S.; Barakat, M.A.; Rashid, J.; Salah, N.; Al-Ghamdi, A.A. Role of N doping on the structural, optical and photocatalytic properties of the silver deposited ZnO thin films. *J. Taiwan Inst. Chem. Eng.* **2016**, *69*, 131–138. [CrossRef]
126. Das, A.; Wary, R.R.; Nair, R.G. Mn-doped ZnO:Role of morphological evolution on enhanced photocatalytic performance. *Energy Rep.* **2020**, *6*, 737–741. [CrossRef]
127. Nie, M.; Liao, J.; Cai, H.; Sun, H.; Xue, Z.; Guo, P.; Wu, M. Photocatalytic property of silver enhanced Ag/ZnO composite catalyst. *Chem. Phys. Lett.* **2021**, *768*, 138394. [CrossRef]
128. Zhou, X.; Ai, C.; Wang, X.; Wu, Z.; Zhang, J. F− surface modified ZnO for enhanced photocatalytic H_2O_2 production and its fs-TAS investigation. *J. Mater.* **2025**, *11*, 100974. [CrossRef]
129. Khanchandani, S.; Kundu, S.; Patra, A.; Ganguli, A.K. Shell Thickness Dependent Photocatalytic Properties of ZnO/CdS Core–Shell Nanorods. *J. Phys. Chem. C* **2012**, *116*, 23653–23662. [CrossRef]
130. Cho, S.; Jang, J.-W.; Kim, J.; Lee, J.S.; Choi, W.; Lee, K.-H. Three-Dimensional Type II ZnO/ZnSe Heterostructures and Their Visible Light Photocatalytic Activities. *Langmuir* **2011**, *27*, 10243–10250. [CrossRef]
131. Naseri, A.; Samadi, M.; Pourjavadi, A.; Ramakrishna, S.; Moshfegh, A.Z. Enhanced photocatalytic activity of ZnO/g-C_3N_4 nanofibers constituting carbonaceous species under simulated sunlight for organic dye removal. *Ceram. Int.* **2021**, *47*, 26185–26196. [CrossRef]
132. Chen, X.; Xu, X.; Cui, J.; Chen, C.; Zhu, X.; Sun, D.; Qian, J. Visible-light driven degradation of tetracycline hydrochloride and 2,4-dichlorophenol by film-like N-carbon@N-ZnO catalyst with three-dimensional interconnected nanofibrous structure. *J. Hazard. Mater.* **2020**, *392*, 122331. [CrossRef]
133. Yuan, Z.; Shi, X.; Chen, K. Preparation and characterization of chitosan/ZnO-Ag composite microcapsules and their applications in solar energy harvesting and electromagnetic interference shielding. *Int. J. Biol. Macromol.* **2024**, *263*, 130285. [CrossRef]
134. Linsebigler, A.L.; Lu, G.; Yates, J.T., Jr. Photocatalysis on TiO_2 Surfaces: Principles, Mechanisms, and Selected Results. *Chem. Rev.* **1995**, *95*, 735–758. [CrossRef]
135. Armakovic, S.J.; Savanovic, M.M.; Armakovic, S. Titanium Dioxide as the Most Used Photocatalyst for Water Purification: An Overview. *Catalysts* **2023**, *13*, 26. [CrossRef]
136. Zhao, K.; Guo, Z.; Wang, J.; Xie, H. Phase change *n*-Octadecane microencapsulated in titanium dioxide nanoparticle-doped polymer for photothermal conversion and photocatalysis. *Sol. Energy* **2023**, *254*, 73–87. [CrossRef]
137. Zhao, A.; Xiao, X.; Hu, Z.-T.; Zhu, W.; Yang, J.; Yang, E.-H. Multifunctional F-doped TiO_2 PCM microcapsules for visible-light-driven photocatalysis and latent heat storage. *Appl. Energy* **2024**, *359*, 122674. [CrossRef]
138. Rawal, S.B.; Chakraborty, A.K.; Lee, W.I. Heterojunction of FeOOH and TiO_2 for the formation of visible light photocatalyst. *Bull. Korean Chem. Soc.* **2009**, *30*, 2613–2616. [CrossRef]
139. Amani-Ghadim, A.R.; Alizadeh, S.; Khodam, F.; Rezvani, Z. Synthesis of rod-like α-FeOOH nanoparticles and its photocatalytic activity in degradation of an azo dye: Empirical kinetic model development. *J. Mol. Catal. A Chem.* **2015**, *408*, 60–68. [CrossRef]
140. Xu, B.; Wei, Z.; Hong, X.; Zhou, Y.; Gan, S.; Shen, M. Preparation and characterization of novel microencapsulated phase change materials with SiO_2/FeOOH as the shell for heat energy storage and photocatalysis. *J. Energy Storage* **2021**, *43*, 103251. [CrossRef]

141. Ren, K.; Yue, S.; Li, C.; Fang, Z.; Gasem, K.A.M.; Leszczynski, J.; Qu, S.; Wang, Z.; Fan, M. Metal halide perovskites for photocatalysis applications. *J. Mater. Chem. A* **2022**, *10*, 407–429. [CrossRef]
142. DuBose, J.T.; Kamat, P.V. Efficacy of Perovskite Photocatalysis: Challenges to Overcome. *ACS Energy Lett.* **2022**, *7*, 1994–2011. [CrossRef]
143. Zhang, H.; Ji, X.; Xu, H.; Zhang, R.; Zhang, H. Design and modification of perovskite materials for photocatalytic performance improvement. *J. Environ. Chem. Eng.* **2023**, *11*, 109056. [CrossRef]
144. Kaur, J.; Peter, S.C. Two-Dimensional Perovskites for Photocatalytic CO_2 Reduction. *Angew. Chem. Int. Ed.* **2025**, *64*, e202418708. [CrossRef]
145. Lakshmanan, P.; Youk, J.H. A comprehensive review of carbon nitride-based catalysts for overall water splitting: Dimensional insights. *Sustain. Mater.Technol.* **2025**, *45*, e01483. [CrossRef]
146. Fernandes, E.; Mazierski, P.; Miodyńska-Melzer, M.; Nikiforow, K.; Klimczuk, T.; Zaleska-Medynska, A.; Martins, R.C.; Gomes, J. Cerium oxide integration and oxygen doping of g-C_3N_4 for boosted solar removal of emerging pollutants and water disinfection. *Chem. Eng. J.* **2025**, *521*, 166993. [CrossRef]
147. Liu, J.; Qi, K.; Xiang, X.; Jamal Sisi, A.; Khataee, A.; Xu, L. Covalent Organic Framework-Based Photocatalysts from Synthesis to Applications. *Energy Environ. Mater.* **2025**, *8*, e70071. [CrossRef]
148. Zhang, J.; Li, X.; Hu, H.; Huang, H.; Li, H.; Sun, X.; Ma, T. Enhancing photocatalytic performance of covalent organic frameworks via ionic polarization. *Nat. Commun.* **2024**, *15*, 9576. [CrossRef]
149. Wang, L.; Zhang, Y. Impact of Interfaces on the Performance of Covalent Organic Frameworks for Photocatalytic Hydrogen Production. *Small* **2024**, *21*, 2408395. [CrossRef]
150. Jablonski, A. Efficiency of Anti-Stokes Fluorescence in Dyes. *Nature* **1933**, *131*, 839–840. [CrossRef]
151. Khoee, S.; Zamani, S.; Tajik, M. An investigation into the role of polarity of diamines in controlling the electron migration mechanism of photoluminescent poly(amide–imide)s. *Spectrochim. Acta Part A* **2009**, *72*, 1054–1061. [CrossRef]
152. Lu, S.; Sui, L.; Liu, J.; Zhu, S.; Chen, A.; Jin, M.; Yang, B. Near-Infrared Photoluminescent Polymer–Carbon Nanodots with Two-Photon Fluorescence. *Adv. Mater.* **2017**, *29*, 1603443. [CrossRef]
153. Montini, T.; Gombac, V.; Hameed, A.; Felisari, L.; Adami, G.; Fornasiero, P. Synthesis, characterization and photocatalytic performance of transition metal tungstates. *Chem. Phys. Lett.* **2010**, *498*, 113–119. [CrossRef]
154. Liu, X.; Guo, Z.; Wang, J.; Xie, H. Fluorescence and Thermal Regulation Using Low-Supercooling Inorganic Microencapsulated Phase-Change Materials. *ACS Appl. Mater. Interfaces* **2023**, *15*, 20444–20457. [CrossRef]
155. Zhang, Y.; Wang, X.; Wu, D. Microencapsulation of *n*-dodecane into zirconia shell doped with rare earth: Design and synthesis of bifunctional microcapsules for photoluminescence enhancement and thermal energy storage. *Energy* **2016**, *97*, 113–126. [CrossRef]
156. Wei, H.; He, F.; Li, Y.; Zhang, Q.; Zhou, Y.; Yan, H.; He, R.; Fan, J.; Yang, W. Bifunctional Paraffin@$CaCO_3$:Ce^{3+} Phase Change Microcapsules for Thermal Energy Storage and Photoluminescence. *ACS Sustain. Chem. Eng.* **2019**, *7*, 18854–18862. [CrossRef]
157. Liu, H.; Shen, H.; Zhang, H.; Wang, X. Development of photoluminescence phase-change microcapsules for comfort thermal regulation and fluorescent recognition applications in advanced textiles. *J. Energy Storage* **2022**, *49*, 104158. [CrossRef]
158. Otaegui, J.R.; Ruiz-Molina, D.; Hernando, J.; Roscini, C. Multidimensional Data Encoding Based on Multicolor Microencapsulated Thermoresponsive Fluorescent Phase Change Materials. *Adv. Funct. Mater.* **2024**, *34*, 2402510. [CrossRef]
159. Du, J.; Sheng, L.; Chen, Q.; Xu, Y.; Li, W.; Wang, X.; Li, M.; Zhang, S.X.-A. Simple and general platform for highly adjustable thermochromic fluorescent materials and multi-feasible applications. *Mater. Horiz.* **2019**, *6*, 1654–1662. [CrossRef]
160. Yu, J.; Liu, H.; Wang, Y.; Li, J.; Wu, D.; Wang, X. Fluorescent sensing system based on molecularly imprinted phase-change microcapsules and carbon quantum dots for high-efficient detection of tetracycline. *J. Colloid Interface Sci.* **2021**, *599*, 332–350. [CrossRef]

Disclaimer/Publisher's Note: The statements, opinions and data contained in all publications are solely those of the individual author(s) and contributor(s) and not of MDPI and/or the editor(s). MDPI and/or the editor(s) disclaim responsibility for any injury to people or property resulting from any ideas, methods, instructions or products referred to in the content.